

Inferring Vector Magnetic Fields from Stokes Profiles of GST/NIRIS Using a Convolutional Neural Network

HAO LIU,^{1,2} YAN XU,^{1,3,4} JIASHENG WANG,^{1,3,4} JU JING,^{1,3,4} CHANG LIU,^{1,3,4} JASON T. L. WANG,^{1,2} AND
HAIMIN WANG^{1,3,4}

¹*Institute for Space Weather Sciences, New Jersey Institute of Technology, University Heights, Newark, NJ 07102-1982, USA*
hl422@njit.edu, yan.xu@njit.edu, jw438@njit.edu, ju.jing@njit.edu, chang.liu@njit.edu, wangj@njit.edu, haimin.wang@njit.edu

²*Department of Computer Science, New Jersey Institute of Technology, University Heights, Newark, NJ 07102-1982, USA*

³*Center for Solar-Terrestrial Research, New Jersey Institute of Technology, University Heights, Newark, NJ 07102-1982, USA*

⁴*Big Bear Solar Observatory, New Jersey Institute of Technology, 40386 North Shore Lane, Big Bear City, CA 92314-9672, USA*

ABSTRACT

We propose a new machine learning approach to Stokes inversion based on a convolutional neural network (CNN) and the Milne-Eddington (ME) method. The Stokes measurements used in this study were taken by the Near InfraRed Imaging Spectropolarimeter (NIRIS) on the 1.6 m Goode Solar Telescope (GST) at the Big Bear Solar Observatory. By learning the latent patterns in the training data prepared by the physics-based ME tool, the proposed CNN method is able to infer vector magnetic fields from the Stokes profiles of GST/NIRIS. Experimental results show that our CNN method produces smoother and cleaner magnetic maps than the widely used ME method. Furthermore, the CNN method is 4~6 times faster than the ME method, and is able to produce vector magnetic fields in near real-time, which is essential to space weather forecasting. Specifically, it takes ~50 seconds for the CNN method to process an image of 720×720 pixels comprising Stokes profiles of GST/NIRIS. Finally, the CNN-inferred results are highly correlated to the ME-calculated results and are closer to the ME's results with the Pearson product-moment correlation coefficient (PPMCC) being closer to 1 on average than those from other machine learning algorithms such as multiple support vector regression and multilayer perceptrons (MLP). In particular, the CNN method outperforms the current best machine learning method (MLP) by 2.6% on average in PPMCC according to our experimental study. Thus, the proposed physics-assisted deep learning-based CNN tool can be considered as an alternative, efficient method for Stokes inversion for high resolution polarimetric observations obtained by GST/NIRIS.

Keywords: Sun: magnetic fields – Methods: data analysis – Techniques: spectroscopic

1. INTRODUCTION

Stokes inversion has been an important yet challenging task in solar physics for decades (Auer et al. 1977; del Toro Iniesta & Ruiz Cobo 1996; Asensio Ramos & de la Cruz Rodríguez 2015). Its purpose is to infer physical parameters such as the total magnetic field strength, inclination and azimuth angles, Doppler shift of the line center and so on from spectropolarimetric data. In general, such an inversion task is accomplished by attempting to find an appropriate forward model that best describes the relationship between the spectral shapes of the four Stokes components and the physical parameters, which is essentially a nonlinear nonconvex inverse problem. In the past, several inversion models have been developed. Based on the Levenberg-Marquardt algorithm (Landolfi et al. 1984; Skumanich & Lites 1987; Press et al. 1991), a simplified model named the Milne-Eddington (ME) method (Auer et al. 1977; Landi Degl'Innocenti 1984) provides an analytical solution for fast evaluation of the required derivatives in the algorithm. Later, a more sophisticated method was introduced by Ruiz Cobo & del Toro Iniesta (1992) based on response functions, which is able to retrieve height dependent information. This method has several different implementations including SPINOR (Frutiger et al. 2000), Helix+ (Lagg et al. 2004) and VFISV (Borrero et al. 2011).

In recent years, with rapid developments of advanced instruments and high-performance computers, powerful telescopes, such as the Daniel K. Inouye Solar Telescope (*DKIST*; McMullin et al. 2012), European Solar Telescope (*EST*; Collados 2008) and Goode Solar Telescope (*GST*; Goode & Cao 2012) at the Big Bear Solar Observatory (BBSO),

can produce data in unprecedented spatial and spectral resolution with high cadence. In order to process these data in a time that is practical on a human timescale, more efficient and stable automated methods are in demand. Many researchers have demonstrated that it is effective and efficient to perform Stokes inversion based on machine learning. For example, [Socas-Navarro et al. \(2001\)](#), [Ruiz Cobo & Asensio Ramos \(2012\)](#), and [Quintero Noda et al. \(2015\)](#) developed methods for transforming Stokes profiles to a low-dimensional space using principal component analysis, which reduces the computational load and makes subsequent inversions faster. [Carroll & Staude \(2001\)](#), [Socas-Navarro \(2003, 2005\)](#), and [Carroll & Kopf \(2008\)](#) employed multilayer perceptrons (MLP) for Stokes inversion, demonstrating the speed, noise tolerance and stability of the MLP. [Rees et al. \(2004\)](#) and [Teng \(2015\)](#) used multiple support vector regression (MSVR) for real-time Stokes inversion. More recently, [Asensio Ramos & Díaz Baso \(2019\)](#) performed Stokes inversion based on convolutional neural networks (CNNs; [LeCun et al. 2015](#)) and applied their techniques to synthetic Stokes profiles obtained from snapshots of three-dimensional magneto-hydrodynamic numerical simulations of different structures of the solar atmosphere.

In this paper, we present a new machine learning method, also based on CNNs, for Stokes inversion on the Near InfraRed Imaging Spectropolarimeter (NIRIS) data ([Cao et al. 2012](#)). Our CNN method differs from that of [Asensio Ramos & Díaz Baso \(2019\)](#) in two ways. First, [Asensio Ramos & Díaz Baso \(2019\)](#) used Stokes spectra synthesized in 3D MHD simulations of the solar atmosphere and employed the CNNs to exploit all the spatial information encoded in a training dataset. In contrast, our method performs pixel-by-pixel inversions, exploiting the spatial information of the Stokes profiles in a pixel. Second, in the synthetic data used by [Asensio Ramos & Díaz Baso \(2019\)](#), each Stokes component has 112 spectral points. In contrast, in our NIRIS data, each Stokes component has 60 spectral points. Due to the different input sizes, the architecture of our CNN is different from those in [Asensio Ramos & Díaz Baso \(2019\)](#).

The rest of this paper is organized as follows. Section 2 describes the NIRIS data used in this study and our data collection scheme. Section 3 details our proposed CNN architecture and algorithm. Section 4 reports experimental results. Section 5 concludes the paper.

2. DATA

The GST/NIRIS is the second generation of the InfraRed Imaging Magnetograph (IRIM; [Cao et al. 2006](#)), offering unprecedented high resolution vector magnetograms of the solar atmosphere from the deepest photosphere through the base of the corona. Its dual Fabry-Pérot etalons provide an 85 arcsec field-of-view (FOV) with a cadence of 1 sec for spectroscopic scan and 10 sec for full Stokes measurements. The system utilizes half the chip to capture two simultaneous polarization states side-by-side, and provides an image scale of $0''.083/\text{pixel}$. It produces full spectroscopic measurements I, Q, U, V (Stokes profiles) at a spectral resolution of 0.01 nm in Fe I 1564.8 nm band, with a typical range of -0.25 to $+0.25$ nm from the line center ([Wang et al. 2015](#); [Xu et al. 2016](#); [Wang et al. 2017](#); [Liu et al. 2018](#); [Xu et al. 2018](#)). Figure 1 illustrates the Stokes I, Q, U, V components of a pixel with a 857 Gauss magnetic field strength, 98 degree inclination angle, and 8 degree azimuth angle calculated by the Milne-Eddington (ME) method ([Auer et al. 1977](#); [Landi Degl'Innocenti 1984](#)). Each Stokes component contains 60 wavelength sampling points.

We consider three active regions (ARs), namely AR 12371, AR 12665 and AR 12673, in four different days. For the AR 12371, we consider ten 990×950 images collected at ten different time points on 2015 June 22; we randomly select one million pixels (data samples) from these ten images to form the training set. Then, again for the AR 12371, we consider ten 720×720 images collected at ten different time points on 2015 June 25; we use the image collected at 20:00:00 UT on 2015 June 25 as the first test set. Next, we consider ten 720×720 images from the AR 12665 collected at ten different time points on 2017 July 13; we use the image collected at 18:35:00 UT on 2017 July 13 as the second test set. Finally, we consider one 720×720 image from the AR 12673 collected at 19:18:00 UT on 2017 September 6, and use this image as the third test set. Each test set (image) has 518400 pixels corresponding to 518400 data samples. The training set and each of the test sets are disjoint. The first test set is of the same active region and within ~ 3 days of the training set, while the second test set and third test set are of different active regions, just over 2 years later. We want to see how well the trained CNN model works on these different test sets.

Each data sample (pixel) is comprised of Stokes I, Q, U, V profiles taken at 60 spectral points. In addition, each data sample has a label, which is the vector magnetic field, including the total magnetic field strength, inclination angle and azimuth angle, calculated by the ME method. During training, the labels of the data samples in the training set are used to train and optimize our CNN model. Because the labels of the training data are created by the physics-based ME method, our CNN model can be considered as a physics-assisted deep learning-based method.

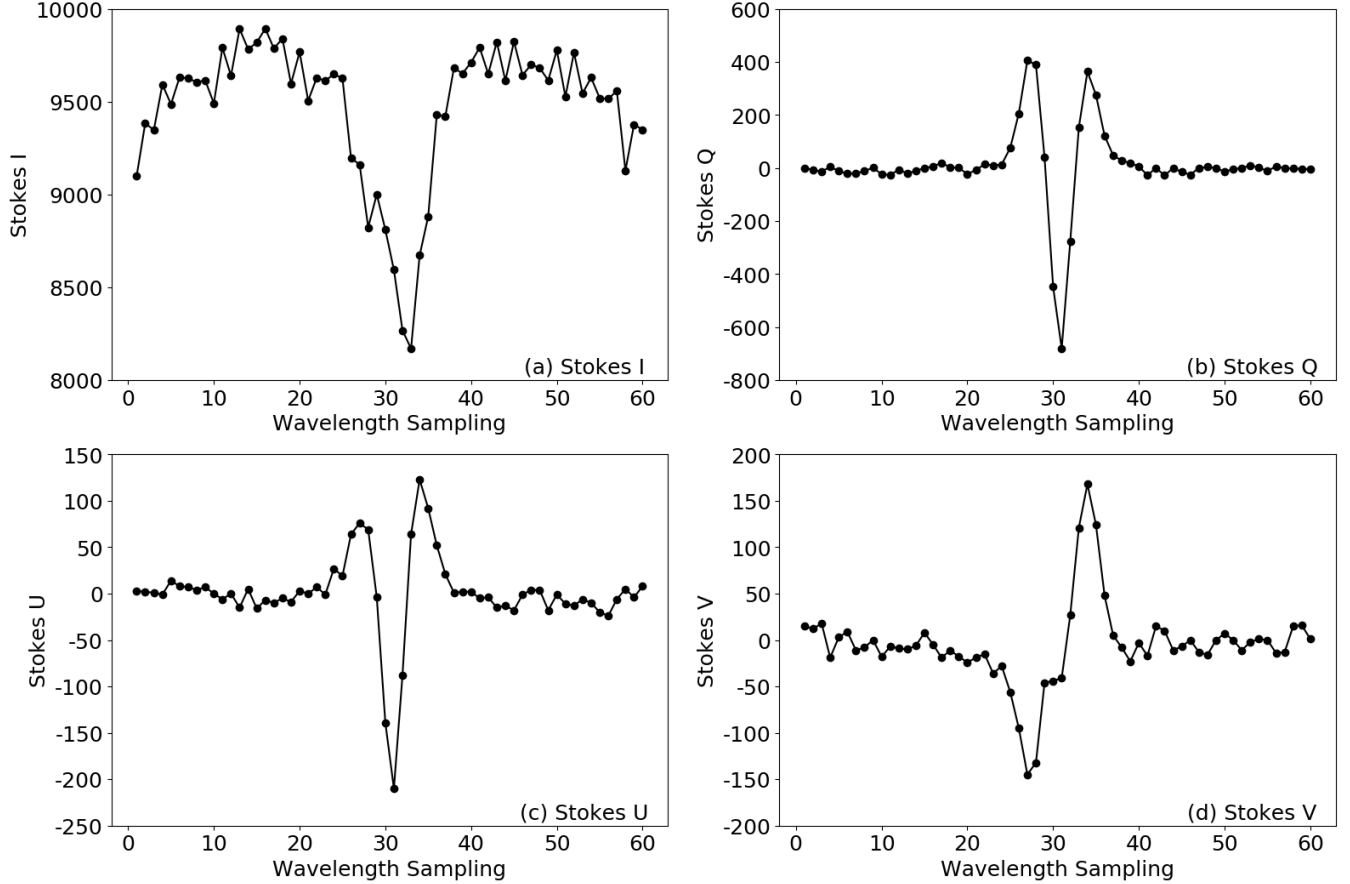


Figure 1. Stokes profiles of a pixel with a 857 Gauss magnetic field strength, 98 degree inclination angle, and 8 degree azimuth angle calculated by the ME method. Each Stokes component has 60 wavelength sampling points.

During testing, we use the trained CNN model to predict or infer the label of a test data sample from the Stokes Q, U, V profiles, calibrated by the Stokes I component (Umno 1956), of the test data sample. We then compare the labels (i.e., vector magnetic fields) inferred by our CNN model with those calculated by the ME method for the test data samples under consideration. Because the Stokes profiles and labels have different units and scales, we normalize them as follows. For the Stokes profiles, we normalize them by dividing them by 1000. For the labels, we normalize the total magnetic field strength by dividing it by 5000, and normalize the inclination angle and azimuth angle by dividing them by π respectively. The two numbers, 1000 and 5000, are used here because most of the Stokes measurements have values between -1000 and $+1000$, and their total magnetic field strengths range from -5000 Gauss to $+5000$ Gauss.

After obtaining the estimated vector magnetic field, which is inferred by our trained model, of a test data sample (pixel), we can derive the three Cartesian components of the magnetic field, namely B_x , B_y and B_z , of the pixel as follows:

$$\begin{cases} B_x = B_{total} \times \sin\phi \times \cos\theta \\ B_y = B_{total} \times \sin\phi \times \sin\theta \\ B_z = B_{total} \times \cos\phi \end{cases} \quad (1)$$

where B_{total} denotes the total magnetic field strength, ϕ is the inclination angle, and θ is the azimuth angle.

3. METHODOLOGY

We use a convolutional neural network (CNN) to infer vector magnetic fields from Stokes profiles of GST/NIRIS. Our CNN model helps in denoising inversions by exploiting the spatial information of the Stokes profiles. Figure 2 presents the architecture of our network. It contains an input layer, three convolutional blocks, two fully connected layers

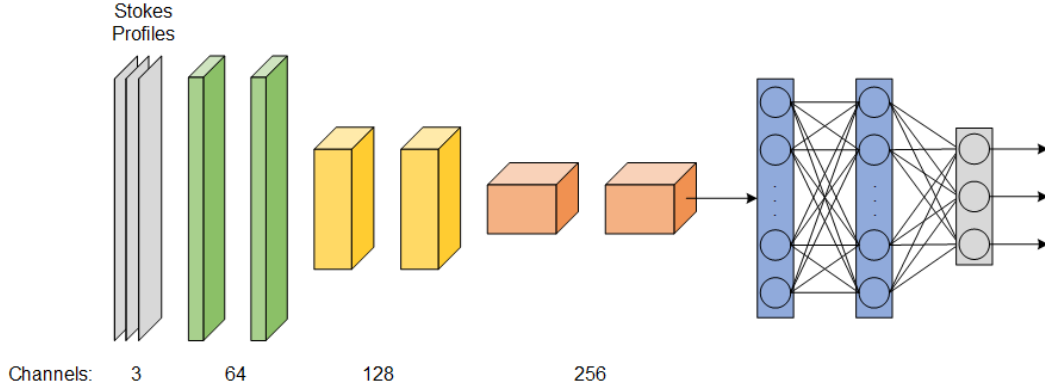


Figure 2. Architecture of our convolutional neural network (CNN). This network is comprised of an input layer, three convolutional blocks, two fully connected layers and an output layer. The input of the CNN is a three-channels sequence of Stokes Q, U, V components each having 60 wavelength sampling points. The intermediate outputs of the three convolutional blocks have 64, 128 and 256 channels respectively. There are 1024 neurons activated by ReLU in both of the two fully connected layers. The output layer has three neurons activated by the Tanh function, where each neuron produces a value in the range $(-1, 1)$ representing the total magnetic field strength, inclination angle and azimuth angle, respectively.

and an output layer. The input layer receives a sequence of Stokes Q, U, V components, each having 60 wavelength sampling points, with 3 channels. Each channel corresponds to a Stokes component respectively.

After the input layer, there are three convolutional blocks with the following structures. The first convolutional block consists of two convolutional layers, which take, as input, the output from the previous layer and filter it with 64 kernels of sizes $3 \times 1 \times 3$ and $3 \times 1 \times 64$ respectively, and a max-pooling layer with a pooling factor of 2. The second convolutional block consists of two convolutional layers with filters of 128 kernels of sizes $3 \times 1 \times 64$ and $3 \times 1 \times 128$ respectively, and a max-pooling layer with a pooling factor of 2. The third convolutional block consists of two convolutional layers with filters of 256 kernels of sizes $3 \times 1 \times 128$ and $3 \times 1 \times 256$ respectively. The third convolutional block does not contain a max-pooling layer.

The activation functions used in both the convolutional layers and fully connected layers are rectified linear units (ReLU; Goodfellow et al. 2016), defined as:

$$\text{ReLU}(x) = \max(0, x) = \begin{cases} x & \text{if } x \geq 0 \\ 0 & \text{if } x < 0 \end{cases} \quad (2)$$

The output of the three convolutional blocks is flattened into a sequence, which is then sent to the two fully connected layers each having 1024 neurons activated by ReLU. Finally, there is an output layer with 3 neurons activated by the hyperbolic tangent function (Tanh; Goodfellow et al. 2016), defined as:

$$\text{Tanh}(x) = \left(\frac{e^x - e^{-x}}{e^x + e^{-x}} \right), \quad (3)$$

where each neuron outputs a value that lies in the range $(-1, 1)$ representing the total magnetic field strength, inclination angle and azimuth angle, respectively. The training of the CNN model is done by optimizing L1 loss defined as follows (Goodfellow et al. 2016):

$$\text{L1 loss} = \frac{1}{N} \sum_{i=1}^N (|y_i^{\text{tot}} - \hat{y}_i^{\text{tot}}| + |y_i^{\text{inc}} - \hat{y}_i^{\text{inc}}| + |y_i^{\text{azi}} - \hat{y}_i^{\text{azi}}|), \quad (4)$$

where $N = 1,000,000$ is the total number of pixels in the training set, and $y_i^{\text{tot}}, y_i^{\text{inc}}, y_i^{\text{azi}}$ ($\hat{y}_i^{\text{tot}}, \hat{y}_i^{\text{inc}}, \hat{y}_i^{\text{azi}}$ respectively) denotes the total magnetic field strength, inclination angle and azimuth angle of the i th pixel calculated by the ME method (inferred by our CNN method, respectively). L1 loss is chosen here because it is efficient and produces good results as shown in Section 4.

Our CNN model is implemented in Python, TensorFlow and Keras. A mini-batch strategy (LeCun et al. 2015; Goodfellow et al. 2016) is used to achieve faster convergence during backpropagation. The optimizer used is Adam

(LeCun et al. 2015; Goodfellow et al. 2016), which is a stochastic gradient descent method. The initial learning rate is set to 0.001 with a learning rate decay of 0.01 over each epoch, β_1 is set to 0.9, and β_2 is set to 0.999. The batch size is set to 256 and the number of epochs is set to 50.

During testing, to infer the physical parameters of each pixel in a test image, we take the Stokes Q, U, V profiles of the pixel and feed them to the trained CNN model. The CNN model will output a three-dimensional vector with normalized values in the range $(-1, 1)$ representing the total magnetic field strength (B_{total}), inclination angle (ϕ) and azimuth angle (θ) respectively. By de-normalization of the values, we can obtain the inferred or estimated B_{total} , ϕ and θ of the pixel. Furthermore, based on the estimated B_{total} , ϕ and θ , we can derive the three Cartesian components of the magnetic field, namely B_x , B_y and B_z , of the pixel using Equation (1).

4. RESULTS

4.1. Performance Metrics

We conducted a series of experiments to evaluate the performance of the proposed CNN model and compare it with related methods based on four performance metrics: mean absolute error (MAE; Sen & Srivastava 1990), percent agreement (PA; McHugh 2012), R-squared (Sen & Srivastava 1990) and Pearson product-moment correlation coefficient (PPMCC; Galton 1886; Pearson 1895). We considered six quantities: total magnetic field strength (B_{total}), inclination angle (ϕ), azimuth angle (θ), B_x , B_y and B_z . For each quantity, we compared its ME-calculated values with our CNN-inferred values and computed the four performance metrics.

The first performance metric is defined as (Sen & Srivastava 1990):

$$\text{MAE} = \frac{1}{N} \sum_{i=1}^N |y_i - \hat{y}_i|, \quad (5)$$

where N is the total number of data samples (pixels) in a test image, and y_i (\hat{y}_i , respectively) denotes the ME-calculated (CNN-inferred, respectively) value for the i th pixel in the test image. This metric is used to quantitatively assess the dissimilarity (distance) between the ME-calculated values and CNN-inferred values in the test image. The smaller the MAE is, the better performance a method has.

The second performance metric is defined as (McHugh 2012):

$$\text{PA} = \frac{M}{N} \times 100\%, \quad (6)$$

where M denotes the total number of agreement pixels in the test image. We say the i th pixel in the test image is an agreement pixel if $|y_i - \hat{y}_i|$ is smaller than a user-specified threshold. (The default thresholds are set to 200 Gauss for B_{total} , B_x , B_y , B_z respectively and 10 degree for ϕ , θ respectively.) This metric is used to quantitatively assess the similarity between the ME-calculated values and CNN-inferred values in the test image. The larger the PA is, the better performance a method has.

The third performance metric is defined as (Sen & Srivastava 1990):

$$\text{R-squared} = 1 - \frac{\sum_{i=1}^N (y_i - \hat{y}_i)^2}{\sum_{i=1}^N (y_i - \bar{y})^2}, \quad (7)$$

where $\bar{y} = \frac{1}{N} \sum_{i=1}^N y_i$ denotes the mean of the ME-calculated values for all the pixels in the test image. The R-squared value, ranging from $-\infty$ to 1, is used to measure the strength of the relationship between the ME-calculated values and CNN-inferred values in the test image. The larger (i.e., the closer to 1) the R-squared value is, the stronger relationship between the ME-calculated values and CNN-inferred values we have.

The fourth performance metric is defined as (Galton 1886; Pearson 1895):

$$\text{PPMCC} = \frac{E[(X - \mu_X)(Y - \mu_Y)]}{\sigma_X \sigma_Y}, \quad (8)$$

where X and Y represent the ME-calculated values and CNN-inferred values respectively, μ_X and μ_Y are the mean of X and Y respectively, σ_X and σ_Y are the standard deviation of X and Y respectively, and $E(\cdot)$ is the expectation. The value of PPMCC ranges from -1 to 1 . A value of 1 means that a linear equation describes the relationship between X

and Y perfectly where all data points lying on a line for which Y increases as X increases. A value of -1 means that all data points lie on a line for which Y decreases as X increases. A value of 0 means that there is no linear correlation between the variables X and Y . We will mainly use PPMCC in our experimental study because it measures the linear correlation between the ME-calculated values and CNN-inferred values, quantifying how well the CNN-inferred values agree with the ME-calculated values in the test image (Galton 1886; Pearson 1895; Sen & Srivastava 1990). The larger (i.e., the closer to 1) the PPMCC is, the better performance a method has. Notice that PA, R-squared and PPMCC do not have units while MAE has units: “Gauss” for B_{total} , B_x , B_y , B_z respectively and “degree” for ϕ (inclination angle), θ (azimuth angle) respectively.

4.2. Results of Using AR 12371 on 2015 June 22 as Training Data

In this experiment, we used the one million data samples (pixels) from AR 12371 collected on 2015 June 22 as the training data to train our CNN model. We then used the trained CNN model to infer vector magnetic fields from the Stokes Q, U, V profiles of the pixels in the three test sets (images) described in Section 2.¹ For comparison purposes, we also used the Milne-Eddington (ME) method (Auer et al. 1977; Landi Degl’Innocenti 1984) to derive the vector magnetic fields of the pixels in the three test images.

Figure 3 (Figure 4, Figure 5 respectively) presents results for the three obtained quantities B_{total} , ϕ (inclination angle) and θ (azimuth angle), displayed from top to bottom in the figure, of the test image with 720×720 pixels from AR 12371 (AR 12665, AR 12673 respectively) collected on 2015 June 25 20:00:00 UT (2017 July 13 18:35:00 UT, 2017 September 6 19:18:00 UT respectively). In all the figures, the first column shows scatter plots for each obtained quantity. The X-axis and Y-axis in each scatter plot represent the values obtained by the ME method and CNN method respectively. The black diagonal line in each scatter plot corresponds to pixels whose ME-calculated values are identical to CNN-inferred values. The second columns in these figures show magnetic maps with 720×720 pixels derived by the ME method. The third columns in the figures show magnetic maps with 720×720 pixels inferred by our CNN method.

Summary of the results. The scatter plots in the figures show that the Stokes inversion results obtained by our CNN method and the ME method are highly correlated. From the top-left panels in Figures 3, 4 and 5, we see that the CNN-inferred B_{total} values are closer to the ME-calculated B_{total} values in the low-field end and are farther from the ME-calculated B_{total} values in the high-field end. The figures also show that the CNN method produces smoother and cleaner magnetic maps than the ME method. There are salt-pepper noise pixels in the magnetic maps produced by the ME method. To help locate the noise pixels, we use percentage difference images in which the value of the i th pixel is equal to $(y_i - \hat{y}_i)/y_i \times 100\%$ where y_i (\hat{y}_i , respectively) denotes the ME-calculated (CNN-inferred, respectively) value for the i th pixel. For example, Figure 6 shows the percentage difference images for the ϕ (inclination angle) maps in Figures 3, 4 and 5. The percentage difference images highlight the locations of the differences between the CNN-inferred ϕ values and ME-calculated ϕ values in the test images. Figure 7 (Figure 8, Figure 9 respectively) in the Appendix presents results for the quantities B_x , B_y and B_z , displayed from top to bottom in the figure, of the test image with 720×720 pixels from AR 12371 (AR 12665, AR 12673 respectively) collected on 2015 June 25 20:00:00 UT (2017 July 13 18:35:00 UT, 2017 September 6 19:18:00 UT respectively).

To quantitatively assess the number of noise pixels in the magnetic maps derived by the ME and CNN methods, we adopt a threshold-based algorithm, which works as follows. We define P to be a noise pixel (outlier) with respect to a user-specified threshold if among P ’s eight neighboring pixels, there are more than four neighboring pixels satisfying the following condition: the difference between the value of a neighboring pixel and the value of P is greater than or equal to the threshold. The default thresholds are set to 500 Gauss for B_{total} , B_x , B_y , B_z respectively and 20 degree for ϕ (inclination angle), θ (azimuth angle) respectively. We define the outlier-difference to be the number of outliers produced by the ME method minus the number of outliers produced by our CNN method. A positive outlier-difference means ME produces more outliers than CNN while a negative outlier-difference means CNN produces more outliers than ME.

Table 1 presents the performance metric values of the CNN method. The results in Table 1 are consistent with those in Figures 3-9. Specifically, the CNN-inferred results are highly correlated to the ME-calculated results with PPMCC values being close to 1. Furthermore, CNN produces smoother magnetic maps with fewer outliers (noise pixels) than the ME method. This happens because among the one million training data samples whose labels are calculated by

¹ The source code and datasets used in the experiment can be downloaded from <https://web.njit.edu/~wangj/CNNStokesInversion/>.

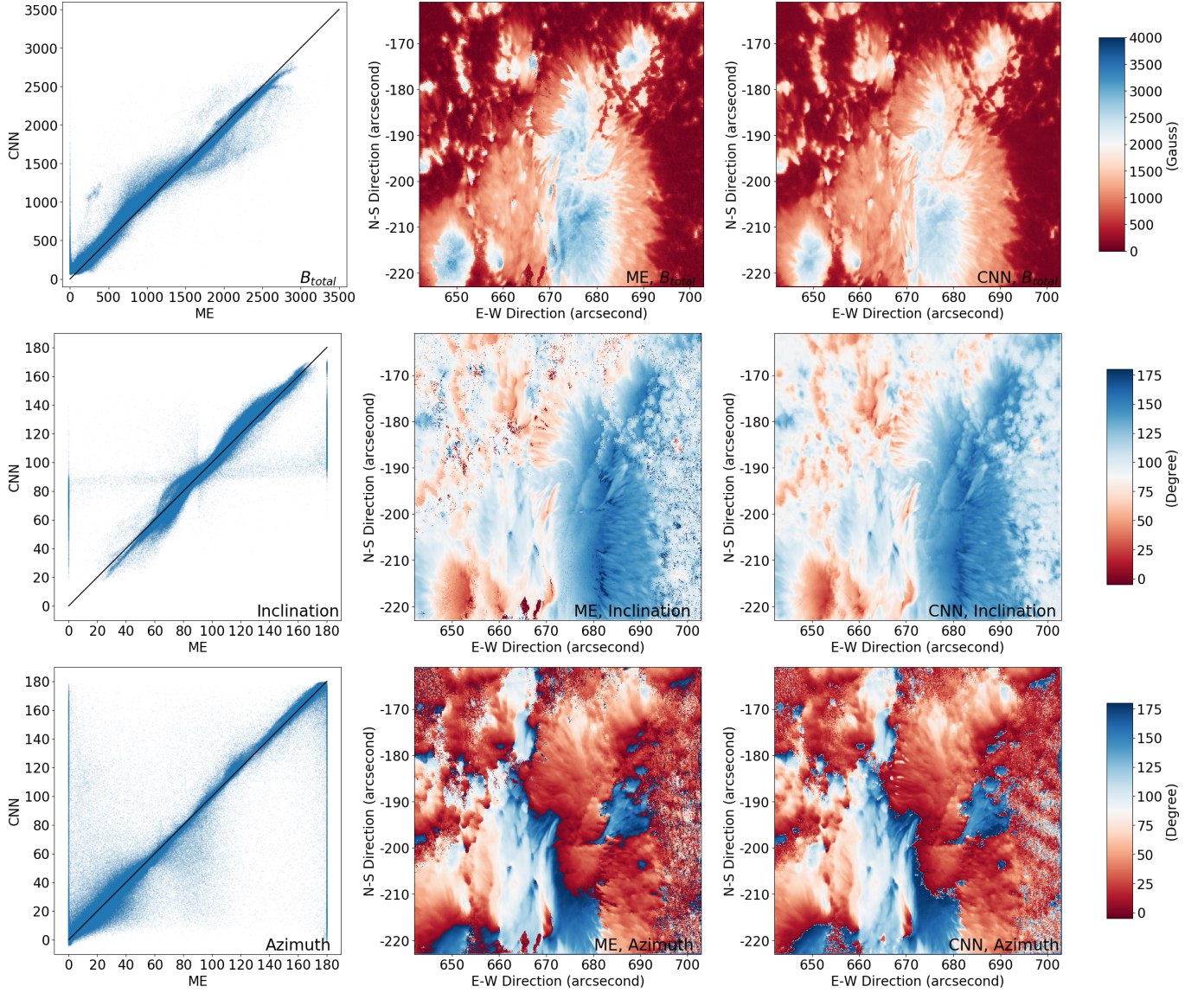


Figure 3. Comparison between the ME and CNN methods for deriving B_{total} , ϕ (inclination angle) and θ (azimuth angle) based on the test image from AR 12371 collected on 2015 June 25 20:00:00 UT where training data were taken from the same AR 12371 on 2015 June 22. Displayed from top to bottom are the results for B_{total} , ϕ (inclination angle) and θ (azimuth angle) respectively. The first column shows scatter plots where the X-axis and Y-axis represent the values obtained by the ME and CNN methods respectively. The black diagonal line in each scatter plot corresponds to pixels whose ME-calculated values are identical to CNN-inferred values. The second column shows magnetic maps derived by the ME method. The third column shows magnetic maps inferred by our CNN method.

the ME method, there are relatively few outliers. The CNN method can learn latent patterns from the majority of the training data samples, which are clean. As a consequence, we obtain a good CNN model capable of producing clean results. Tables 5 and 6 in the Appendix present the performance metric values for the test images from AR 12371 and AR 12665 collected at ten different time points on 2015 June 25 and 2017 July 13 respectively. The results in these tables are consistent with those in Table 1.

Comparison with related methods. To further understand the behavior of our CNN method and compare it with related machine learning algorithms, we conduct a cross-validation study as follows. We partition the training set of one million data samples from AR 12371 on 2015 June 22 into 10 equal-sized folds. For every two training folds i and j , $i \neq j$, fold i and fold j are disjoint. The first test set contains the ten 720×720 images, also from AR 12371, collected on 2015 June 25. These test images are numbered from 1 to 10. In run i , $1 \leq i \leq 10$, all training

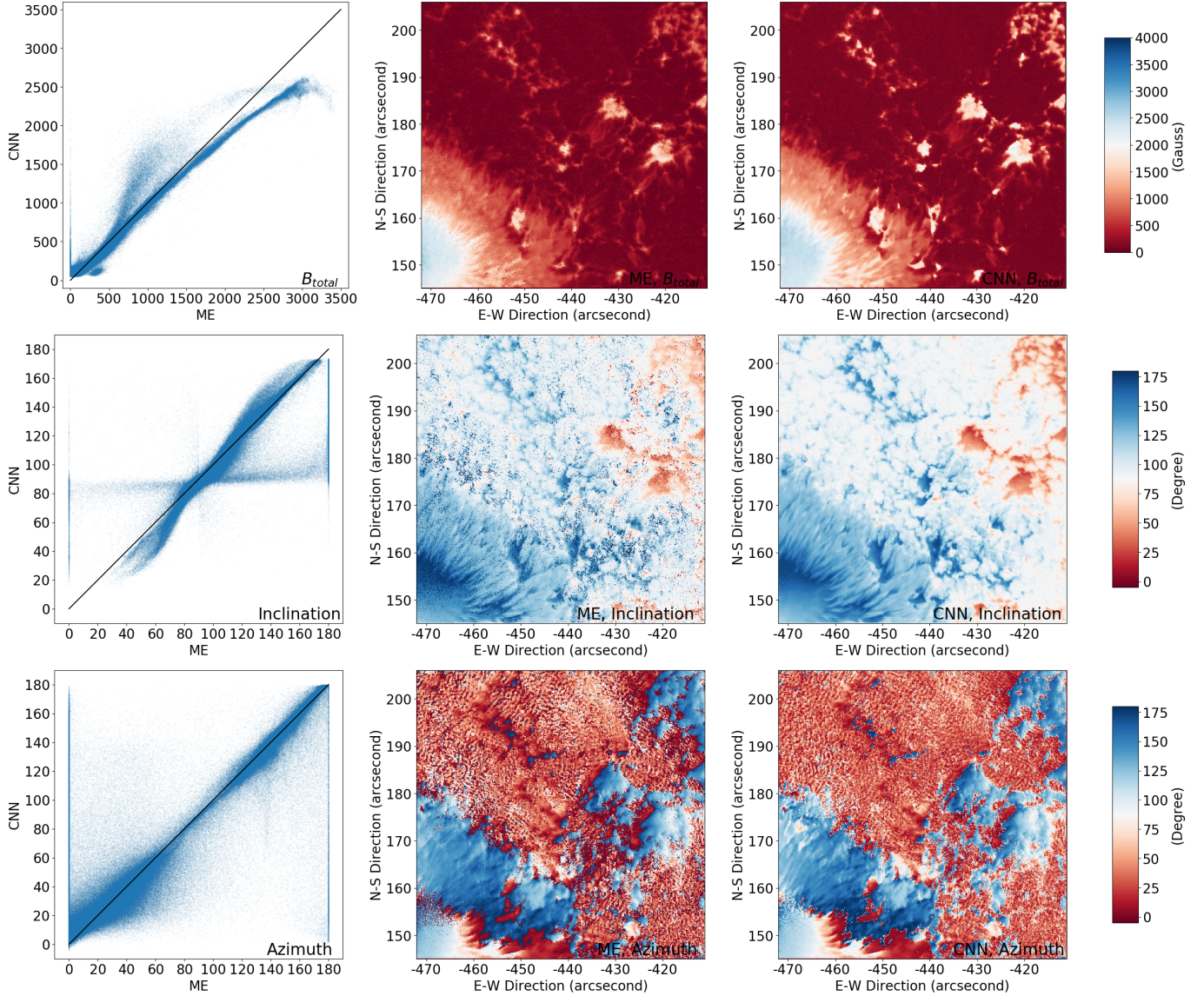


Figure 4. Comparison between the ME and CNN methods for deriving B_{total} , ϕ (inclination angle) and θ (azimuth angle) based on the test image from AR 12665 collected on 2017 July 13 18:35:00 UT where training data were taken from AR 12371 on 2015 June 22. Displayed from top to bottom are the results for B_{total} , ϕ (inclination angle) and θ (azimuth angle) respectively. The first column shows scatter plots where the X-axis and Y-axis represent the values obtained by the ME and CNN methods respectively. The black diagonal line in each scatter plot corresponds to pixels whose ME-calculated values are identical to CNN-inferred values. The second column shows magnetic maps derived by the ME method. The third column shows magnetic maps inferred by our CNN method.

data samples except those in training fold i are used to train a machine learning model, and the trained model is then used to make predictions on test image i . We calculate the performance metrics MAE, PA, R-squared, PPMCC and outlier-difference based on the predictions made in run i . There are 10 runs. The means and standard deviations over the 10 runs are calculated and recorded. We also conduct the same cross-validation study for the second test set containing the ten 720×720 images from AR 12665 collected on 2017 July 13, and the third test set containing the 720×720 image from AR 12673 collected on 2017 September 6. The third test set has only one image, and hence in each run, the same test image is used.

The related machine learning algorithms considered here include multiple support vector regression (MSVR; Rees et al. 2004; Teng 2015) and multilayer perceptrons (MLP; Carroll & Staude 2001; Socas-Navarro 2003, 2005; Carroll & Kopf 2008). The MSVR method uses the radial basis function (RBF) kernel. The MLP model consists of an

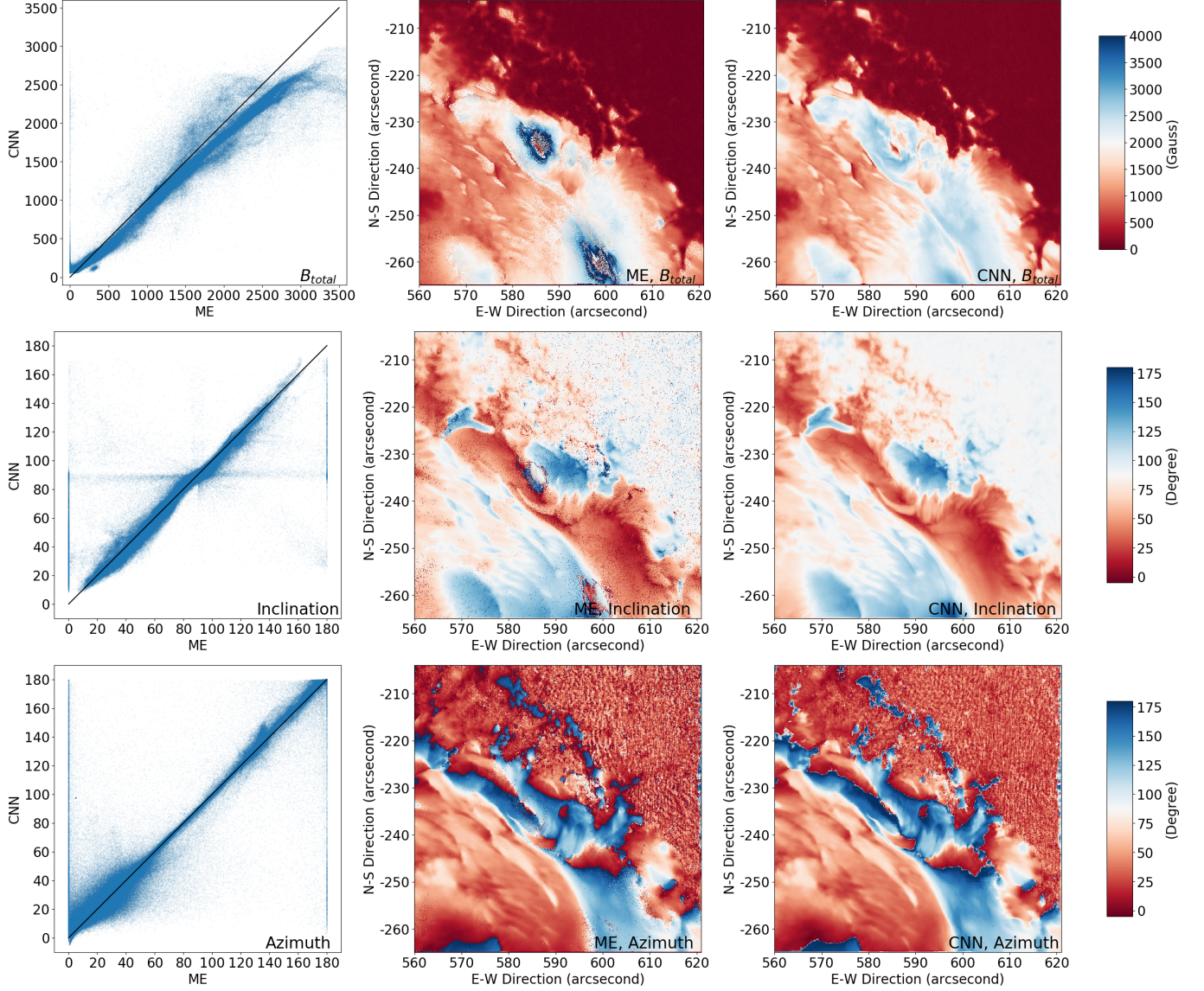


Figure 5. Comparison between the ME and CNN methods for deriving B_{total} , ϕ (inclination angle) and θ (azimuth angle) based on the test image from AR 12673 collected on 2017 September 6 19:18:00 UT where training data were taken from AR 12371 on 2015 June 22. Displayed from top to bottom are the results for B_{total} , ϕ (inclination angle) and θ (azimuth angle) respectively. The first column shows scatter plots where the X-axis and Y-axis represent the values obtained by the ME and CNN methods respectively. The black diagonal line in each scatter plot corresponds to pixels whose ME-calculated values are identical to CNN-inferred values. The second column shows magnetic maps derived by the ME method. The third column shows magnetic maps inferred by our CNN method.

input layer, an output layer and two hidden layers both with 1024 neurons. Table 2 (Table 3, Table 4 respectively) presents the mean MAE, PA, R-squared, PPMCC, outlier-difference and standard deviation for each quantity B_{total} , B_x , B_y , B_z , ϕ (inclination angle), θ (azimuth angle) inferred by each of the three machine learning methods MSVR, MLP and our CNN for the first (second, third respectively) test set. In the tables, PA, R-squared, PPMCC and outlier-difference do not have units while MAE has units: “Gauss” for B_{total} , B_x , B_y , B_z respectively and “degree” for ϕ (inclination angle), θ (azimuth angle) respectively. It can be seen from the tables that the CNN-inferred results are highly correlated to the ME-calculated results and are closer to the ME’s results with PPMCC values being closer to 1 on average than those from the other two machine learning methods. In particular, based on the calculations on the six quantities B_{total} , B_x , B_y , B_z , ϕ (inclination angle) and θ (azimuth angle) in Tables 2-4, our CNN method

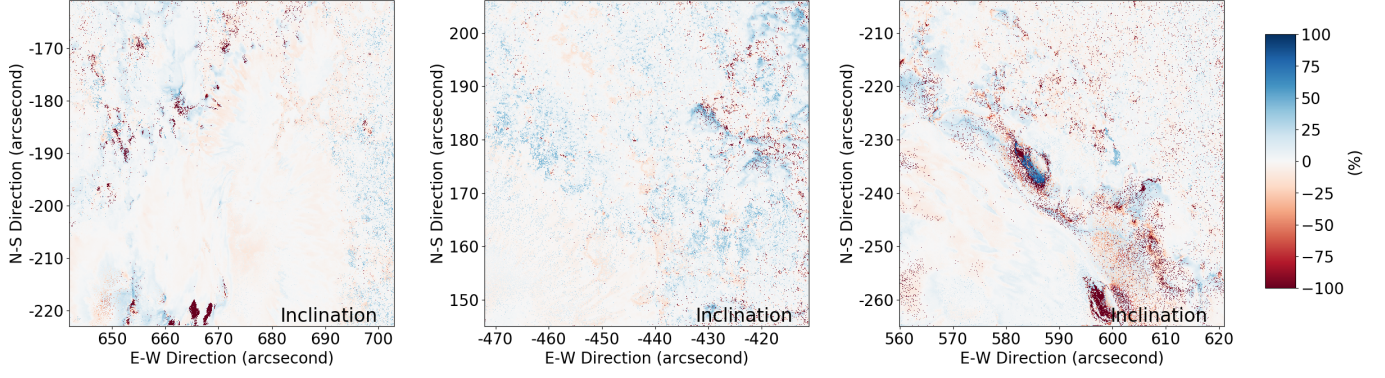


Figure 6. Percentage difference images for the ϕ (inclination angle) maps. The first column shows the percentage difference image based on the test image from AR 12371 collected on 2015 June 25 20:00:00 UT. The second column shows the percentage difference image based on the test image from AR 12665 collected on 2017 July 13 18:35:00 UT. The third column shows the percentage difference image based on the test image from AR 12673 collected on 2017 September 6 19:18:00 UT. These percentage difference images highlight the locations of the differences between the CNN-inferred ϕ values and ME-calculated ϕ values in the three test images.

Table 1. Performance Metric Values of Our CNN Method Based on the Test Images from Three Active Regions

		B_{total}	B_x	B_y	B_z	ϕ	θ
2015-06-25 20:00:00 UT (AR 12371)	MAE	86.660	88.997	66.140	55.653	4.867	11.136
	PA	91.6%	91.3%	95.2%	94.7%	92.2%	79.1%
	R-squared	0.963	0.936	0.901	0.976	0.838	0.720
	PPMCC	0.983	0.968	0.951	0.989	0.916	0.853
	Outlier-difference	2959	4380	-770	1050	15108	7219
2017-07-13 18:35:00 UT (AR 12665)	MAE	73.684	71.555	51.170	49.023	7.573	17.437
	PA	91.5%	93.3%	96.4%	92.6%	84.8%	60.6%
	R-squared	0.950	0.841	0.851	0.941	0.663	0.665
	PPMCC	0.976	0.918	0.926	0.971	0.827	0.821
	Outlier-difference	3801	7280	3413	2478	35649	28274
2017-09-06 19:18:00 UT (AR 12673)	MAE	193.680	146.100	124.783	136.892	5.497	9.009
	PA	75.0%	80.1%	86.2%	87.2%	91.3%	79.1%
	R-squared	0.841	0.884	0.777	0.736	0.776	0.807
	PPMCC	0.935	0.943	0.888	0.859	0.881	0.902
	Outlier-difference	19651	22317	16592	12950	21951	14265

Notes.

^a The performance metric values in the table are obtained by training the CNN model using one million pixels from AR 12371 collected on 2015 June 22 and then applying the trained model to the test image from AR 12371 collected on 2015 June 25 20:00:00 UT (AR 12665 collected on 2017 July 13 18:35:00 UT, and AR 12673 collected on 2017 September 6 19:18:00 UT, respectively).

^b A positive outlier-difference means ME produces more outliers than CNN while a negative outlier-difference means CNN produces more outliers than ME.

outperforms the current best machine learning method (MLP) by 2.6% on average in PPMCC. However, there is no definite conclusion about outlier-differences among the three machine learning methods.

4.3. Results of Using Different Active Regions as Training Data

In the previous subsection we use data points (pixels) from AR 12371 on 2015 June 22 as training data. In this subsection we conduct additional experiments by varying training data as follows. There are four datasets D_1 , D_2 , D_3 , D_4 containing the images from AR 12371 on 2015 June 22, AR 12371 on 2015 June 25, AR 12665 on 2017 July 13, and AR 12673 on 2017 September 6 respectively. In each experiment we randomly select one million pixels (data

Table 2. Performance Metric Values of MSVR, MLP and Our CNN Method Based on the Test Set from AR 12371 Collected on 2015 June 25

		B_{total}	B_x	B_y	B_z	ϕ	θ
MAE	MSVR	437.02 (27.44)	712.02 (19.03)	706.51 (12.24)	339.26 (17.86)	23.02 (0.73)	84.43 (1.53)
	MLP	115.68 (5.15)	109.44 (7.60)	86.08 (4.80)	80.62 (4.19)	5.85 (0.31)	12.29 (1.72)
	CNN	81.57 (3.66)	76.56 (5.63)	58.83 (2.86)	52.18 (2.22)	4.54 (0.23)	9.34 (1.04)
PA	MSVR	34.7% (0.5%)	48.4% (1.0%)	44.6% (1.1%)	15.2% (1.5%)	5.6% (0.2%)	4.1% (0.5%)
	MLP	86.2% (0.7%)	88.4% (0.8%)	91.5% (0.5%)	89.5% (0.7%)	89.4% (1.0%)	76.7% (1.0%)
	CNN	91.6% (0.7%)	92.5% (0.8%)	96.1% (0.5%)	95.1% (0.4%)	93.6% (0.6%)	81.4% (1.4%)
R-squared	MSVR	0.45 (0.05)	-0.92 (0.07)	-5.34 (0.37)	0.28 (0.08)	-0.09 (0.03)	-2.80 (0.16)
	MLP	0.92 (0.01)	0.91 (0.01)	0.85 (0.01)	0.93 (0.01)	0.80 (0.01)	0.73 (0.04)
	CNN	0.97 (0.01)	0.94 (0.01)	0.93 (0.01)	0.97 (0.01)	0.83 (0.01)	0.76 (0.03)
PPMCC	MSVR	0.82 (0.01)	-0.09 (0.04)	-0.10 (0.08)	0.89 (0.01)	0.85 (0.01)	0.48 (0.03)
	MLP	0.97 (0.01)	0.96 (0.01)	0.93 (0.01)	0.97 (0.01)	0.91 (0.01)	0.86 (0.02)
	CNN	0.98 (0.01)	0.97 (0.01)	0.96 (0.01)	0.99 (0.01)	0.91 (0.01)	0.88 (0.02)
Outlier-difference	MSVR	2572 (945)	3009 (511)	-1794 (555)	-2038 (688)	13864 (887)	38828 (2083)
	MLP	3056 (823)	3587 (679)	-208 (166)	1417 (403)	14495 (877)	13526 (2480)
	CNN	3060 (809)	3415 (488)	-419 (235)	1436 (380)	14503 (883)	12645 (2930)

Notes.^a Each number in the table represents the average value of ten experiments.^b Standard deviations are enclosed in parentheses.^c The best PPMCC values achieved by the three machine learning methods are highlighted in boldface.^d A positive outlier-difference means ME produces more outliers than a machine learning method while a negative outlier-difference means the machine learning method produces more outliers than ME.**Table 3.** Performance Metric Values of MSVR, MLP and Our CNN Method Based on the Test Set from AR 12665 Collected on 2017 July 13

		B_{total}	B_x	B_y	B_z	ϕ	θ
MAE	MSVR	387.23 (9.67)	582.00 (65.91)	36.15 (9.34)	209.48 (21.31)	23.09 (1.16)	120.30 (23.96)
	MLP	108.99 (17.69)	90.04 (5.95)	76.68 (3.25)	66.71 (18.89)	7.67 (0.97)	23.38 (4.95)
	CNN	87.70 (10.69)	79.27 (3.60)	58.04 (3.05)	53.26 (13.44)	7.26 (0.80)	19.94 (4.25)
PA	MSVR	19.7% (1.4%)	5.3% (2.2%)	7.8% (1.8%)	78.9% (1.3%)	9.2% (0.8%)	0.5% (0.5%)
	MLP	87.0% (2.4%)	89.9% (0.9%)	94.5% (1.1%)	91.9% (1.9%)	85.8% (1.8%)	51.2% (5.7%)
	CNN	90.8% (1.3%)	92.4% (0.5%)	96.4% (0.8%)	93.8% (1.2%)	87.7% (1.8%)	60.0% (3.7%)
R-squared	MSVR	0.24 (0.27)	-3.37 (1.53)	-2.39 (0.56)	0.54 (0.12)	0.13 (0.09)	-5.67 (3.98)
	MLP	0.85 (0.04)	0.77 (0.04)	0.71 (0.06)	0.86 (0.06)	0.68 (0.05)	0.49 (0.12)
	CNN	0.90 (0.02)	0.80 (0.03)	0.79 (0.05)	0.89 (0.04)	0.70 (0.04)	0.50 (0.14)
PPMCC	MSVR	0.73 (0.10)	0.18 (0.06)	0.52 (0.08)	0.84 (0.03)	0.76 (0.04)	0.35 (0.14)
	MLP	0.95 (0.01)	0.89 (0.02)	0.86 (0.04)	0.94 (0.02)	0.84 (0.03)	0.71 (0.08)
	CNN	0.96 (0.01)	0.89 (0.02)	0.89 (0.03)	0.95 (0.02)	0.85 (0.03)	0.72 (0.09)
Outlier-difference	MSVR	5448 (1026)	6767 (2603)	3142 (1633)	4052 (864)	34672 (7581)	93448 (19733)
	MLP	5668 (1108)	6623 (2620)	3127 (1674)	4185 (928)	34716 (7959)	39277 (14562)
	CNN	5600 (1128)	6267 (2557)	2953 (1583)	4137 (915)	34721 (7945)	24276 (12194)

Notes.^a Each number in the table represents the average value of ten experiments.^b Standard deviations are enclosed in parentheses.^c The best PPMCC values achieved by the three machine learning methods are highlighted in boldface.^d A positive outlier-difference means ME produces more outliers than a machine learning method while a negative outlier-difference means the machine learning method produces more outliers than ME.

Table 4. Performance Metric Values of MSVR, MLP and Our CNN Method Based on the Test Set from AR 12673 Collected on 2017 September 6

		B_{total}	B_x	B_y	B_z	ϕ	θ
MAE	MSVR	549.84 (0.01)	851.67 (0.01)	1079.51 (0.01)	709.89 (0.01)	73.19 (0.01)	56.87 (0.01)
	MLP	339.40 (8.48)	206.18 (6.98)	203.56 (5.43)	223.20 (5.43)	7.35 (0.14)	13.23 (0.17)
	CNN	198.92 (3.94)	150.57 (2.17)	128.04 (1.63)	139.30 (4.40)	5.57 (0.12)	9.27 (0.20)
PA	MSVR	17.7% (0.1%)	39.7% (0.1%)	43.9% (0.1%)	6.9% (0.1%)	2.3% (0.1%)	12.9% (0.1%)
	MLP	55.9% (1.3%)	70.4% (1.5%)	67.9% (0.8%)	73.5% (0.8%)	82.6% (1.1%)	66.0% (0.7%)
	CNN	73.6% (0.4%)	80.4% (0.4%)	84.9% (0.2%)	85.7% (1.5%)	90.9% (0.3%)	78.4% (0.5%)
R-squared	MSVR	0.45 (0.01)	-1.37 (0.01)	-7.11 (0.01)	-0.05 (0.01)	-5.49 (0.01)	-1.10 (0.01)
	MLP	0.60 (0.01)	0.80 (0.01)	0.57 (0.01)	0.65 (0.01)	0.76 (0.01)	0.77 (0.01)
	CNN	0.84 (0.01)	0.87 (0.01)	0.79 (0.01)	0.74 (0.01)	0.78 (0.01)	0.80 (0.01)
PPMCC	MSVR	0.81 (0.01)	-0.18 (0.01)	-0.31 (0.01)	0.56 (0.01)	0.81 (0.01)	0.54 (0.01)
	MLP	0.85 (0.01)	0.92 (0.01)	0.81 (0.01)	0.82 (0.01)	0.88 (0.01)	0.88 (0.01)
	CNN	0.93 (0.01)	0.94 (0.01)	0.89 (0.01)	0.86 (0.01)	0.88 (0.01)	0.90 (0.01)
Outlier-difference	MSVR	19154 (0)	21841 (0)	15980 (0)	12306 (0)	21734 (0)	32424 (0)
	MLP	19632 (20)	22346 (20)	16780 (38)	12941 (8)	21918 (10)	20692 (552)
	CNN	19664 (11)	22234 (46)	16534 (35)	12965 (7)	21950 (7)	14294 (1436)

Notes.

^a Each number in the table represents the average value of ten experiments.

^b Standard deviations are enclosed in parentheses.

^c The best PPMCC values achieved by the three machine learning methods are highlighted in boldface.

^d A positive outlier-difference means ME produces more outliers than a machine learning method while a negative outlier-difference means the machine learning method produces more outliers than ME.

samples) from one or more datasets to form a training set. The CNN model is trained on this training set and the trained model is then used to perform Stokes inversion on a test image. This test image must be from a dataset that is different from those datasets used to construct the training set. The time point for the test image is 17:33:00 UT on 2015 June 22, 20:00:00 UT on 2015 June 25, 18:35:00 UT on 2017 July 13, and 19:18:00 UT on 2017 September 6 respectively. We use $D_x^{\text{train}} \rightarrow D_w^{\text{test}}$ ($D_{x,y}^{\text{train}} \rightarrow D_w^{\text{test}}$, $D_{x,y,z}^{\text{train}} \rightarrow D_w^{\text{test}}$ respectively) to represent the experiment that uses training data samples from D_x (training data samples from D_x and D_y , training data samples from D_x , D_y and D_z respectively) and test data samples (pixels) from D_w where $1 \leq x, y, z, w \leq 4$. Because D_4 has only one 720×720 image with 518400 pixels, D_4 alone is not used as a training set. Hence, there are 25 experiments in total. In each experiment, we calculate the performance metrics MAE, PA, R-squared, PPMCC and outlier-difference. Tables 7–10 in the Appendix present the experimental results. Major findings based on these tables are summarized below.

1. Our CNN-inferred results and ME-calculated results are highly correlated and close to each other with a PPMCC of ~ 0.9 or higher for the total magnetic field strength, regardless of whether the training and test data used by the CNN method are from the same active region (AR) or different ARs, or whether the training and test data are close (e.g., within ~ 3 days) or distant (e.g., over 2 years) in time. This finding can be seen from Tables 7–10 where the PPMCC of B_{total} in $D_2^{\text{train}} \rightarrow D_1^{\text{test}}$ ($D_3^{\text{train}} \rightarrow D_1^{\text{test}}$, $D_1^{\text{train}} \rightarrow D_2^{\text{test}}$, $D_3^{\text{train}} \rightarrow D_2^{\text{test}}$, $D_1^{\text{train}} \rightarrow D_3^{\text{test}}$, $D_2^{\text{train}} \rightarrow D_3^{\text{test}}$, $D_1^{\text{train}} \rightarrow D_4^{\text{test}}$, $D_2^{\text{train}} \rightarrow D_4^{\text{test}}$, and $D_3^{\text{train}} \rightarrow D_4^{\text{test}}$, respectively) is 0.956 (0.924, 0.983, 0.951, 0.976, 0.979, 0.936, 0.927, and 0.896, respectively).

2. With respect to the same test image, using the training data from the same AR in which the test image is taken yields a better result with a higher PPMCC than using the training and test data that are from different ARs. This finding can be seen from Tables 7 and 8 where the PPMCC of B_{total} in $D_2^{\text{train}} \rightarrow D_1^{\text{test}}$ is 0.956, which is greater than the PPMCC of B_{total} , 0.924, in $D_3^{\text{train}} \rightarrow D_1^{\text{test}}$. Moreover, the PPMCC of B_{total} in $D_1^{\text{train}} \rightarrow D_2^{\text{test}}$ is 0.983, which is greater than the PPMCC of B_{total} , 0.951, in $D_3^{\text{train}} \rightarrow D_2^{\text{test}}$.

3. However, with respect to the same test image, using the training and test data that are close in time does not necessarily yield a better result than using the training and test data that are distant in time. This finding can be seen from Table 10 where the PPMCC of B_{total} in $D_1^{\text{train}} \rightarrow D_4^{\text{test}}$ is 0.936, which is greater than the PPMCC of B_{total} , 0.896, in $D_3^{\text{train}} \rightarrow D_4^{\text{test}}$, though D_3 is closer to D_4 than D_1 in time.

4. From Tables 7-10, we can see that the CNN-inferred results have much fewer outliers than the ME-calculated results for all of B_{total} , B_x , B_y , B_z , ϕ , θ in all the experiments except for B_y in Table 8. This finding is consistent with the results reported in Table 1.

5. DISCUSSION AND CONCLUSIONS

We develop a new machine learning method to infer vector magnetic fields from Stokes profiles of GST/NIRIS based on a convolutional neural network (CNN) and the Milne-Eddington (ME) method. We then conduct a series of experiments to evaluate the performance of our method. First, we use data samples (pixels) from AR 12371 collected on 2015 June 22 to train the CNN model where the labels (i.e., vector magnetic fields) of the training data samples are calculated by the ME method. Next, we use the trained model to infer vector magnetic fields from Stokes profiles of pixels in three different unseen test sets. The first test set contains image data from AR 12371 collected on 2015 June 25. The second test set contains image data from AR 12665 collected on 2017 July 13. The third test set contains image data from AR 12673 collected on 2017 September 6. We compare our CNN method with the ME method and two related machine learning algorithms, multiple support vector regression (MSVR) and multilayer perceptrons (MLP), on the three test sets. Finally, we conduct more experiments by varying training data to get different trained models and applying the models to different test data.

Our findings based on these experiments are consistent, which are summarized as follows:

1. Our CNN method produces smoother and cleaner magnetic maps with fewer outliers (noise pixels) than the ME method.
2. It takes ~ 50 seconds for the CNN method to process an image of 720×720 pixels comprising Stokes profiles of GST/NIRIS, which is 4 \sim 6 times faster than the current version of the ME method. The ability of producing vector magnetic fields in near real-time is essential to space weather forecasting.
3. Our CNN-inferred results and ME-calculated results are highly correlated and close to each other with a PPMCC of ~ 0.9 or higher for the total magnetic field strength, regardless of whether the training and test data used by the CNN method are from the same active region (AR) or different ARs, or whether the training and test data are close (e.g., within ~ 3 days) or distant (e.g., over 2 years) in time. With respect to the same test image, using the training data from the same AR in which the test image is taken yields a better result with a higher PPMCC than using the training and test data that are from different ARs. Hence, for a given test image, it is recommended to adopt the CNN model trained on the same AR from which the test image is collected.
4. The CNN-inferred results are closer to the ME-calculated results with PPMCC values being closer to 1 on average than those from the related machine learning methods MSVR and MLP. In particular, the CNN method outperforms the current best machine learning method (MLP) by 2.6% on average in PPMCC. This happens because the CNN method is able to exploit the spatial information of the Stokes profiles, and learn latent patterns between the Stokes profiles and ME-calculated vector magnetic fields in a better way.

Based on these findings, we conclude that the proposed CNN model can be considered as an alternative, efficient method for Stokes inversion for high resolution polarimetric observations obtained by GST/NIRIS. More accurate and efficient Stokes inversion will improve near real-time prediction of space weather in the future as it prepares more accurate magnetic boundary conditions at the solar surface quickly. With the advent of big and complex observational data gathered from diverse instruments such as BBSO/GST and the upcoming Daniel K. Inouye Solar Telescope (DKIST), it is expected that our physics-assisted deep learning-based CNN tool will be a useful utility for processing and analyzing the data.

We thank the referees for very helpful and thoughtful comments. The data used in this study were obtained with GST at BBSO, which is operated by New Jersey Institute of Technology. Obtaining the excellent data would not have been possible without the help of the BBSO team. The BBSO operation is supported by NJIT and NSF grant AGS-1821294. The GST operation is partly supported by the Korea Astronomy and Space Science Institute and Seoul National University. The related machine learning algorithms studied here were implemented in Python. This work was supported by NSF grant AGS-1927578. Y.X., J.J., C.L. and H.W. acknowledge the support of NASA under grants NNX16AF72G, 80NSSC17K0016, 80NSSC18K0673 and 80NSSC18K1705.

Facilities: Big Bear Solar Observatory

APPENDIX

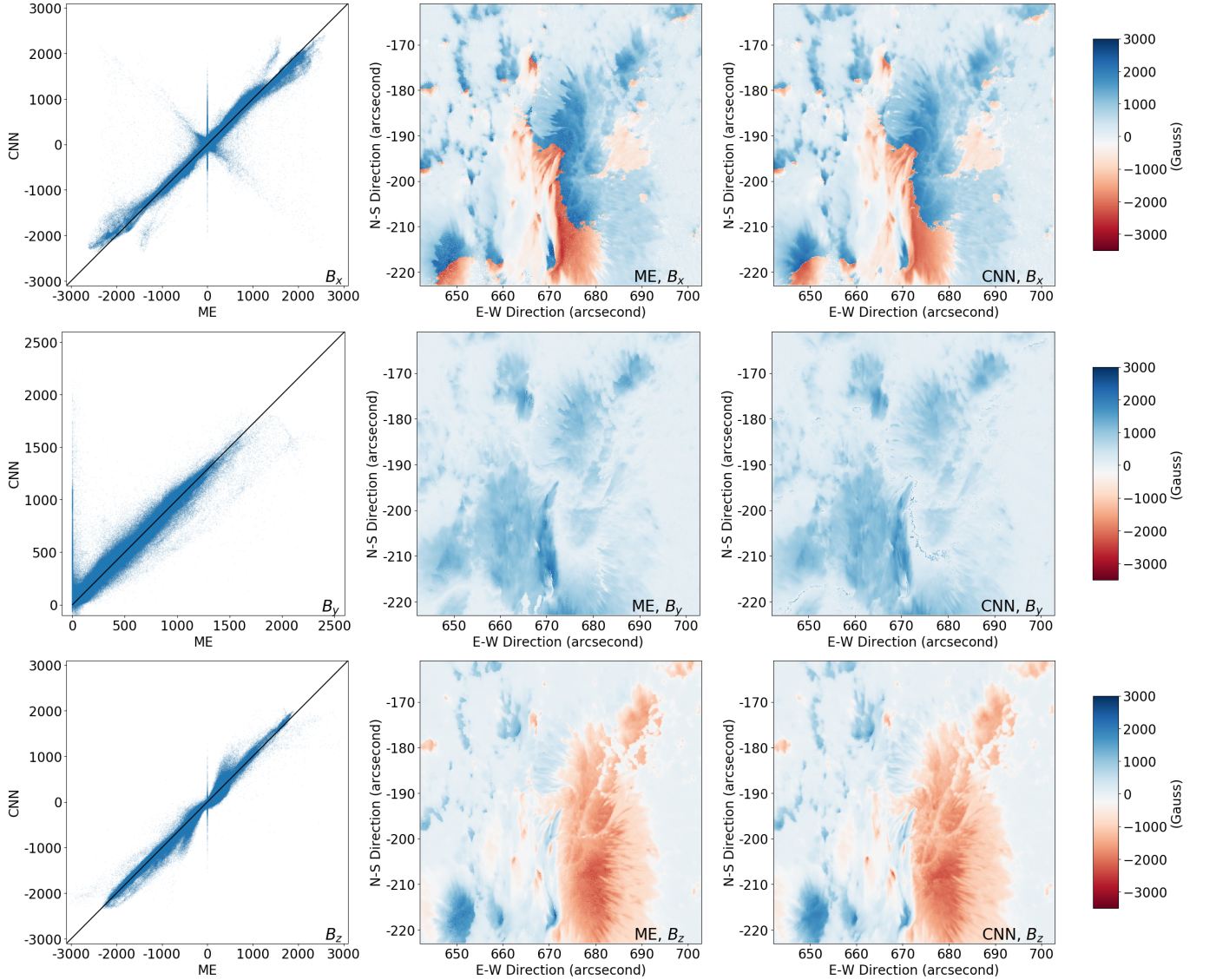


Figure 7. Comparison between the ME and CNN methods for deriving B_x , B_y and B_z based on the test image from AR 12371 collected on 2015 June 25 20:00:00 UT where training data were taken from the same AR 12371 on 2015 June 22. Displayed from top to bottom are the results for B_x , B_y and B_z respectively. The first column shows scatter plots where the X-axis and Y-axis represent the values obtained by the ME and CNN methods respectively. The black diagonal line in each scatter plot corresponds to pixels whose ME-calculated values are identical to CNN-inferred values. The second column shows magnetic maps derived by the ME method. The third column shows magnetic maps inferred by our CNN method.

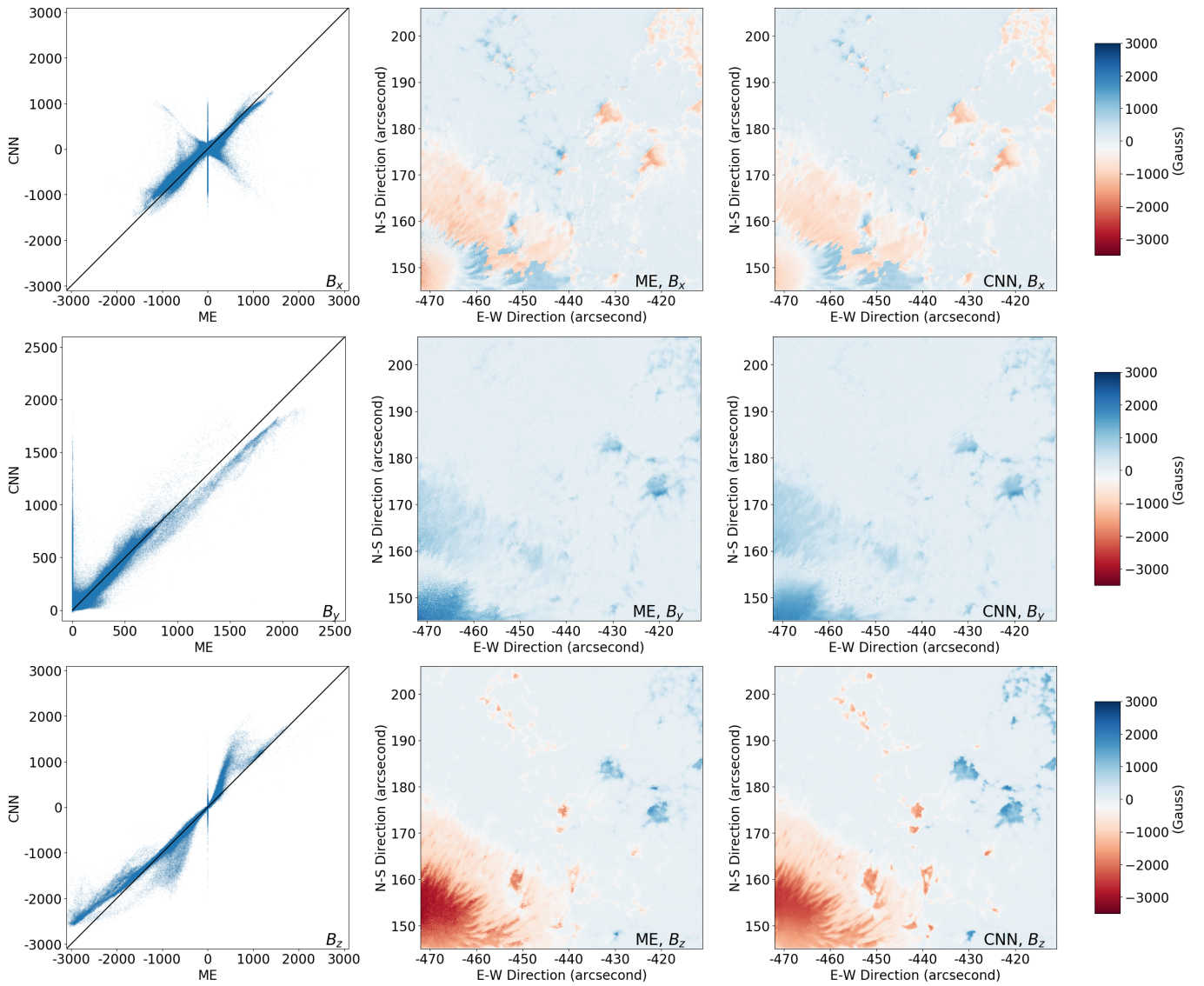


Figure 8. Comparison between the ME and CNN methods for deriving B_x , B_y and B_z based on the test image from AR 12665 collected on 2017 July 13 18:35:00 UT where training data were taken from AR 12371 on 2015 June 22. Displayed from top to bottom are the results for B_x , B_y and B_z respectively. The first column shows scatter plots where the X-axis and Y-axis represent the values obtained by the ME and CNN methods respectively. The black diagonal line in each scatter plot corresponds to pixels whose ME-calculated values are identical to CNN-inferred values. The second column shows magnetic maps derived by the ME method. The third column shows magnetic maps inferred by our CNN method.

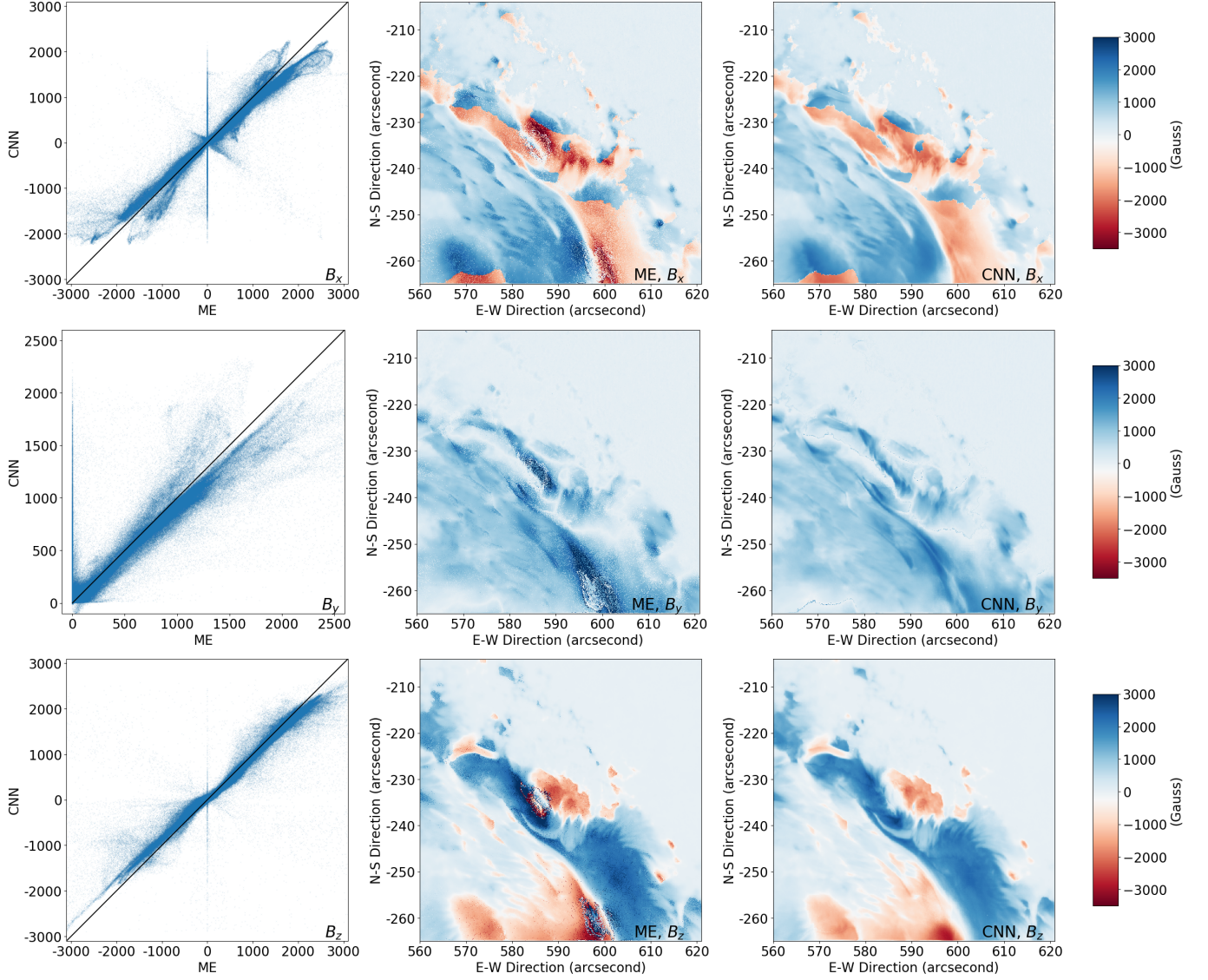


Figure 9. Comparison between the ME and CNN methods for deriving B_x , B_y and B_z based on the test image from AR 12673 collected on 2017 September 6 19:18:00 UT where training data were taken from AR 12371 on 2015 June 22. Displayed from top to bottom are the results for B_x , B_y and B_z respectively. The first column shows scatter plots where the X-axis and Y-axis represent the values obtained by the ME and CNN methods respectively. The black diagonal line in each scatter plot corresponds to pixels whose ME-calculated values are identical to CNN-inferred values. The second column shows magnetic maps derived by the ME method. The third column shows magnetic maps inferred by our CNN method.

Table 5. Performance Metric Values of Our CNN Method Based on the Test Images from AR 12371 Collected at Ten Different Time Points on 2015 June 25

		B_{total}	B_x	B_y	B_z	ϕ	θ	
2015-06-25 (AR 12371)	17:02:00 UT	MAE	79.916	72.753	61.458	53.999	4.578	9.069
		PA	91.9%	93.4%	95.3%	94.6%	93.6%	81.3%
		R-squared	0.965	0.935	0.921	0.968	0.823	0.769
		PPMCC	0.983	0.968	0.961	0.984	0.908	0.879
		Outlier-difference	3935	3881	159	1857	14543	18746
	17:20:00 UT	MAE	86.211	74.157	56.345	54.512	4.254	8.416
		PA	90.2%	92.0%	96.6%	94.4%	94.1%	81.9%
		R-squared	0.961	0.941	0.932	0.966	0.833	0.8797
		PPMCC	0.982	0.971	0.968	0.984	0.913	0.895
		Outlier-difference	5148	3754	-263	2225	13631	14329
	17:41:00 UT	MAE	75.772	68.146	57.255	47.984	4.184	8.376
		PA	92.4%	93.6%	96.1%	95.5%	93.8%	82.5%
		R-squared	0.968	0.947	0.925	0.974	0.847	0.795
		PPMCC	0.985	0.974	0.963	0.987	0.920	0.893
		Outlier-difference	2958	2995	-555	1596	12989	13302
	18:00:00 UT	MAE	77.941	71.767	57.802	50.538	4.498	8.586
		PA	92.6%	93.6%	96.7%	95.4%	93.9%	82.4%
		R-squared	0.970	0.943	0.927	0.974	0.825	0.786
		PPMCC	0.987	0.972	0.966	0.987	0.909	0.888
		Outlier-difference	2813	3036	-630	1639	14735	15265
	18:20:00 UT	MAE	80.294	74.324	56.363	49.600	4.278	8.389
		PA	91.9%	92.5%	96.5%	95.7%	94.5%	83.2%
		R-squared	0.965	0.940	0.931	0.975	0.839	0.788
		PPMCC	0.984	0.970	0.967	0.988	0.917	0.889
		Outlier-difference	2754	2840	-432	1407	13432	12845
	18:40:00 UT	MAE	82.176	77.420	57.013	52.885	4.760	8.948
		PA	91.2%	92.0%	96.4%	94.8%	93.7%	82.2%
		R-squared	0.964	0.942	0.933	0.972	0.822	0.770
		PPMCC	0.984	0.971	0.967	0.987	0.907	0.881
		Outlier-difference	2508	2863	-389	1253	15026	10675
	19:00:00 UT	MAE	79.144	76.014	57.960	52.950	4.716	9.507
		PA	91.7%	92.8%	96.1%	94.9%	93.7%	80.8%
		R-squared	0.967	0.943	0.925	0.975	0.828	0.757
		PPMCC	0.985	0.972	0.964	0.990	0.911	0.872
		Outlier-difference	2450	3166	-424	1125	15383	11646
	19:22:00 UT	MAE	86.917	79.777	59.833	51.695	4.470	9.586
		PA	90.6%	92.3%	95.9%	95.4%	93.3%	81.9%
		R-squared	0.962	0.939	0.924	0.975	0.837	0.742
		PPMCC	0.983	0.970	0.964	0.988	0.915	0.865
		Outlier-difference	2644	3508	-392	1297	14243	11326
19:41:00 UT	MAE	80.683	82.218	58.095	51.991	4.775	11.341	
	PA	91.7%	91.8%	96.3%	95.5%	93.1%	78.8%	
	R-squared	0.966	0.935	0.928	0.974	0.827	0.706	
	PPMCC	0.984	0.968	0.965	0.988	0.910	0.845	
	Outlier-difference	2426	3722	-495	908	15939	11092	
20:00:00 UT	MAE	86.660	88.997	66.140	55.653	4.867	11.136	
	PA	91.6%	91.3%	95.2%	94.7%	92.2%	79.1%	
	R-squared	0.963	0.936	0.901	0.976	0.838	0.720	
	PPMCC	0.983	0.968	0.951	0.989	0.916	0.853	
	Outlier-difference	2959	4380	-770	1050	15108	7219	

Table 6. Performance Metric Values of Our CNN Method Based on the Test Images from AR 12665 Collected at Ten Different Time Points on 2017 July 13

		B_{total}	B_x	B_y	B_z	ϕ	θ	
2017-07-13 (AR 12665)	17:18:00 UT	MAE	96.763	77.228	59.555	65.277	6.995	15.623
		PA	89.9%	93.5%	95.7%	92.7%	88.5%	62.2%
		R-squared	0.895	0.796	0.726	0.875	0.716	0.686
		PPMCC	0.961	0.893	0.857	0.947	0.851	0.834
		Outlier-difference	5612	8931	5341	4805	36440	39816
	17:54:00 UT	MAE	108.101	86.635	60.292	83.230	8.276	16.899
		PA	90.8%	92.3%	95.6%	92.8%	86.0%	60.8%
		R-squared	0.866	0.745	0.695	0.789	0.647	0.677
		PPMCC	0.953	0.864	0.838	0.902	0.814	0.829
		Outlier-difference	5430	11516	5702	5728	45541	41897
	18:25:00 UT	MAE	95.509	81.222	59.119	66.639	7.984	17.809
		PA	89.6%	92.2%	95.7%	91.9%	86.5%	60.1%
		R-squared	0.914	0.822	0.792	0.874	0.661	0.664
		PPMCC	0.971	0.907	0.893	0.947	0.824	0.820
		Outlier-difference	3874	8158	4134	3657	42169	39937
	18:35:00 UT	MAE	73.684	71.555	51.170	49.023	7.573	17.437
		PA	91.5%	93.3%	96.4%	92.6%	84.8%	60.6%
		R-squared	0.950	0.841	0.851	0.941	0.663	0.665
		PPMCC	0.976	0.918	0.926	0.971	0.827	0.821
		Outlier-difference	3801	7280	3413	2478	35649	28274
	20:19:00 UT	MAE	75.811	78.550	55.695	38.701	8.014	26.263
		PA	92.8%	92.1%	97.4%	95.7%	86.6%	55.6%
		R-squared	0.915	0.826	0.831	0.930	0.680	0.456
		PPMCC	0.960	0.910	0.916	0.966	0.831	0.693
		Outlier-difference	5089	4479	1900	3341	41315	12610
	20:52:00 UT	MAE	77.201	78.757	56.624	41.618	7.979	26.759
		PA	92.6%	92.1%	97.6%	95.1%	86.4%	54.3%
		R-squared	0.914	0.805	0.827	0.926	0.682	0.401
		PPMCC	0.957	0.897	0.913	0.963	0.834	0.656
		Outlier-difference	5878	4499	1788	4019	38418	10550
	21:20:00 UT	MAE	80.011	77.987	57.099	42.847	7.200	25.012
		PA	92.2%	92.4%	97.4%	94.9%	88.3%	55.1%
		R-squared	0.901	0.799	0.805	0.918	0.710	0.352
		PPMCC	0.952	0.895	0.901	0.961	0.851	0.624
		Outlier-difference	5997	4505	1771	3992	33783	15985
	21:48:00 UT	MAE	84.746	78.946	57.296	43.822	6.471	21.160
		PA	89.6%	91.9%	97.0%	94.9%	90.1%	60.7%
		R-squared	0.895	0.791	0.808	0.917	0.728	0.380
		PPMCC	0.953	0.891	0.901	0.963	0.859	0.643
		Outlier-difference	6234	4556	1938	3916	28967	19769
22:18:00 UT	MAE	95.769	81.151	61.962	52.672	5.890	16.784	
	PA	88.8%	91.7%	95.7%	93.6%	90.3%	64.6%	
	R-squared	0.869	0.771	0.779	0.893	0.776	0.364	
	PPMCC	0.942	0.881	0.884	0.952	0.888	0.640	
	Outlier-difference	7325	4238	1721	5022	22740	15454	
22:39:00 UT	MAE	89.352	80.647	61.617	48.760	6.226	15.683	
	PA	90.3%	92.0%	95.8%	94.4%	89.4%	65.9%	
	R-squared	0.889	0.774	0.751	0.913	0.775	0.399	
	PPMCC	0.951	0.885	0.868	0.961	0.889	0.664	
	Outlier-difference	6757	4506	1826	4408	22186	18471	

Table 7. Performance Metric Values of Our CNN Method Obtained by Using D_1 to Form Test Data and Different Combinations of D_2, D_3, D_4 to Form Training Data

		B_{total}	B_x	B_y	B_z	ϕ	θ
MAE	$D_2^{train} \rightarrow D_1^{test}$	112.104	70.871	77.554	83.761	5.040	10.286
	$D_3^{train} \rightarrow D_1^{test}$	168.905	96.727	116.505	112.322	5.724	11.874
	$D_{2,3}^{train} \rightarrow D_1^{test}$	99.187	74.859	75.777	81.588	5.330	10.330
	$D_{2,4}^{train} \rightarrow D_1^{test}$	96.981	78.739	77.672	70.458	5.111	11.356
	$D_{3,4}^{train} \rightarrow D_1^{test}$	137.511	87.619	105.794	83.560	5.315	11.086
	$D_{2,3,4}^{train} \rightarrow D_1^{test}$	97.594	73.092	75.116	74.675	5.095	10.258
PA	$D_2^{train} \rightarrow D_1^{test}$	88.5%	93.6%	92.4%	90.8%	90.6%	78.0%
	$D_3^{train} \rightarrow D_1^{test}$	71.8%	89.5%	80.8%	85.7%	89.0%	78.6%
	$D_{2,3}^{train} \rightarrow D_1^{test}$	89.2%	92.7%	92.5%	91.2%	89.6%	78.5%
	$D_{2,4}^{train} \rightarrow D_1^{test}$	90.0%	92.2%	92.6%	92.4%	90.5%	76.3%
	$D_{3,4}^{train} \rightarrow D_1^{test}$	81.7%	91.3%	87.6%	90.5%	90.2%	78.9%
	$D_{2,3,4}^{train} \rightarrow D_1^{test}$	89.7%	92.7%	92.5%	92.3%	90.2%	79.1%
R-squared	$D_2^{train} \rightarrow D_1^{test}$	0.903	0.913	0.878	0.955	0.867	0.710
	$D_3^{train} \rightarrow D_1^{test}$	0.845	0.860	0.810	0.929	0.867	0.576
	$D_{2,3}^{train} \rightarrow D_1^{test}$	0.907	0.910	0.875	0.953	0.868	0.706
	$D_{2,4}^{train} \rightarrow D_1^{test}$	0.909	0.899	0.862	0.962	0.861	0.657
	$D_{3,4}^{train} \rightarrow D_1^{test}$	0.886	0.888	0.830	0.954	0.864	0.661
	$D_{2,3,4}^{train} \rightarrow D_1^{test}$	0.904	0.908	0.874	0.956	0.869	0.701
PPMCC	$D_2^{train} \rightarrow D_1^{test}$	0.956	0.956	0.937	0.982	0.935	0.847
	$D_3^{train} \rightarrow D_1^{test}$	0.924	0.933	0.929	0.965	0.933	0.780
	$D_{2,3}^{train} \rightarrow D_1^{test}$	0.954	0.956	0.936	0.980	0.936	0.846
	$D_{2,4}^{train} \rightarrow D_1^{test}$	0.954	0.951	0.932	0.982	0.932	0.822
	$D_{3,4}^{train} \rightarrow D_1^{test}$	0.946	0.947	0.931	0.978	0.932	0.821
	$D_{2,3,4}^{train} \rightarrow D_1^{test}$	0.952	0.955	0.935	0.980	0.936	0.843
Outlier-difference	$D_2^{train} \rightarrow D_1^{test}$	9396	4718	3419	6808	33687	22528
	$D_3^{train} \rightarrow D_1^{test}$	9527	3625	3355	6554	33202	27896
	$D_{2,3}^{train} \rightarrow D_1^{test}$	9266	4045	3120	6760	33114	25720
	$D_{2,4}^{train} \rightarrow D_1^{test}$	9185	4480	3086	6782	33754	24704
	$D_{3,4}^{train} \rightarrow D_1^{test}$	9160	3921	2878	6771	33671	33627
	$D_{2,3,4}^{train} \rightarrow D_1^{test}$	8668	4528	3301	6813	33691	26670

Table 8. Performance Metric Values of Our CNN Method Obtained by Using D_2 to Form Test Data and Different Combinations of D_1, D_3, D_4 to Form Training Data

		B_{total}	B_x	B_y	B_z	ϕ	θ
MAE	$D_1^{train} \rightarrow D_2^{test}$	86.660	88.997	66.140	55.653	4.867	11.136
	$D_3^{train} \rightarrow D_2^{test}$	165.558	132.399	92.024	109.629	6.157	12.191
	$D_{1,3}^{train} \rightarrow D_2^{test}$	83.631	86.654	61.893	51.414	4.650	10.949
	$D_{1,4}^{train} \rightarrow D_2^{test}$	90.098	88.494	63.458	60.282	4.935	10.595
	$D_{3,4}^{train} \rightarrow D_2^{test}$	133.132	104.756	85.091	79.925	5.250	11.805
	$D_{1,3,4}^{train} \rightarrow D_2^{test}$	79.830	84.662	59.412	50.448	4.736	11.023
PA	$D_1^{train} \rightarrow D_2^{test}$	91.6%	91.3%	95.2%	94.7%	92.2%	79.1%
	$D_3^{train} \rightarrow D_2^{test}$	69.4%	81.8%	87.8%	81.2%	87.3%	74.9%
	$D_{1,3}^{train} \rightarrow D_2^{test}$	89.7%	90.5%	95.5%	95.3%	93.3%	79.2%
	$D_{1,4}^{train} \rightarrow D_2^{test}$	89.0%	90.5%	95.1%	94.0%	92.6%	80.2%
	$D_{3,4}^{train} \rightarrow D_2^{test}$	79.0%	88.1%	89.7%	89.7%	92.3%	76.8%
	$D_{1,3,4}^{train} \rightarrow D_2^{test}$	91.9%	92.0%	95.7%	96.0%	93.1%	78.8%
R-squared	$D_1^{train} \rightarrow D_2^{test}$	0.963	0.936	0.901	0.976	0.838	0.720
	$D_3^{train} \rightarrow D_2^{test}$	0.893	0.899	0.850	0.928	0.828	0.695
	$D_{1,3}^{train} \rightarrow D_2^{test}$	0.962	0.937	0.914	0.979	0.844	0.724
	$D_{1,4}^{train} \rightarrow D_2^{test}$	0.956	0.936	0.907	0.972	0.839	0.727
	$D_{3,4}^{train} \rightarrow D_2^{test}$	0.937	0.927	0.858	0.964	0.837	0.711
	$D_{1,3,4}^{train} \rightarrow D_2^{test}$	0.966	0.938	0.918	0.980	0.842	0.724
PPMCC	$D_1^{train} \rightarrow D_2^{test}$	0.983	0.968	0.951	0.989	0.916	0.853
	$D_3^{train} \rightarrow D_2^{test}$	0.951	0.949	0.939	0.982	0.915	0.846
	$D_{1,3}^{train} \rightarrow D_2^{test}$	0.982	0.968	0.957	0.990	0.919	0.855
	$D_{1,4}^{train} \rightarrow D_2^{test}$	0.981	0.968	0.955	0.988	0.916	0.856
	$D_{3,4}^{train} \rightarrow D_2^{test}$	0.982	0.968	0.954	0.989	0.916	0.850
	$D_{1,3,4}^{train} \rightarrow D_2^{test}$	0.984	0.969	0.960	0.990	0.918	0.855
Outlier-difference	$D_1^{train} \rightarrow D_2^{test}$	2959	4380	-770	1050	15108	7219
	$D_3^{train} \rightarrow D_2^{test}$	2950	3904	-246	1032	15054	10038
	$D_{1,3}^{train} \rightarrow D_2^{test}$	2948	4354	-666	1053	15108	7392
	$D_{1,4}^{train} \rightarrow D_2^{test}$	2954	4231	-574	1055	15108	11235
	$D_{3,4}^{train} \rightarrow D_2^{test}$	2953	3926	-533	1057	15000	9161
	$D_{1,3,4}^{train} \rightarrow D_2^{test}$	2959	4380	-631	1053	15108	9410

Table 9. Performance Metric Values of Our CNN Method Obtained by Using D_3 to Form Test Data and Different Combinations of D_1, D_2, D_4 to Form Training Data

		B_{total}	B_x	B_y	B_z	ϕ	θ
MAE	$D_1^{train} \rightarrow D_3^{test}$	73.683	71.555	51.170	49.023	7.573	17.437
	$D_2^{train} \rightarrow D_3^{test}$	98.412	83.441	55.674	58.326	7.330	18.232
	$D_{1,2}^{train} \rightarrow D_3^{test}$	70.574	68.776	48.467	43.919	7.381	16.780
	$D_{1,4}^{train} \rightarrow D_3^{test}$	68.492	66.340	48.593	48.398	7.394	15.661
	$D_{2,4}^{train} \rightarrow D_3^{test}$	68.903	64.068	44.475	46.860	6.539	14.911
	$D_{1,2,4}^{train} \rightarrow D_3^{test}$	68.876	67.419	48.227	43.239	7.250	16.839
PA	$D_1^{train} \rightarrow D_3^{test}$	91.5%	93.3%	96.4%	92.6%	84.8%	60.6%
	$D_2^{train} \rightarrow D_3^{test}$	90.1%	92.3%	95.7%	93.9%	87.0%	54.8%
	$D_{1,2}^{train} \rightarrow D_3^{test}$	92.8%	93.8%	96.6%	94.1%	85.6%	61.3%
	$D_{1,4}^{train} \rightarrow D_3^{test}$	91.1%	93.1%	95.8%	93.5%	84.2%	65.7%
	$D_{2,4}^{train} \rightarrow D_3^{test}$	93.1%	93.7%	96.7%	93.8%	87.1%	68.0%
	$D_{1,2,4}^{train} \rightarrow D_3^{test}$	91.5%	93.9%	96.7%	93.1%	86.2%	61.9%
R-squared	$D_1^{train} \rightarrow D_3^{test}$	0.950	0.841	0.851	0.941	0.663	0.665
	$D_2^{train} \rightarrow D_3^{test}$	0.926	0.830	0.850	0.924	0.661	0.678
	$D_{1,2}^{train} \rightarrow D_3^{test}$	0.957	0.849	0.857	0.955	0.665	0.688
	$D_{1,4}^{train} \rightarrow D_3^{test}$	0.951	0.848	0.855	0.944	0.667	0.698
	$D_{2,4}^{train} \rightarrow D_3^{test}$	0.952	0.845	0.860	0.946	0.703	0.696
	$D_{1,2,4}^{train} \rightarrow D_3^{test}$	0.959	0.848	0.858	0.956	0.672	0.680
PPMCC	$D_1^{train} \rightarrow D_3^{test}$	0.976	0.918	0.926	0.971	0.827	0.821
	$D_2^{train} \rightarrow D_3^{test}$	0.979	0.913	0.923	0.978	0.829	0.829
	$D_{1,2}^{train} \rightarrow D_3^{test}$	0.979	0.921	0.928	0.978	0.828	0.834
	$D_{1,4}^{train} \rightarrow D_3^{test}$	0.975	0.921	0.926	0.973	0.828	0.839
	$D_{2,4}^{train} \rightarrow D_3^{test}$	0.976	0.922	0.929	0.973	0.843	0.844
	$D_{1,2,4}^{train} \rightarrow D_3^{test}$	0.980	0.921	0.928	0.978	0.831	0.830
Outlier-difference	$D_1^{train} \rightarrow D_3^{test}$	3801	7280	3413	2478	35649	28274
	$D_2^{train} \rightarrow D_3^{test}$	3837	7284	3545	2497	35661	27447
	$D_{1,2}^{train} \rightarrow D_3^{test}$	3800	7252	3433	2480	35647	25888
	$D_{1,4}^{train} \rightarrow D_3^{test}$	3812	7200	3405	2481	35645	31320
	$D_{2,4}^{train} \rightarrow D_3^{test}$	3824	6873	3494	2496	35657	26492
	$D_{1,2,4}^{train} \rightarrow D_3^{test}$	3801	7371	3463	2490	35645	24124

Table 10. Performance Metric Values of Our CNN Method Obtained by Using D_4 to Form Test Data and Different Combinations of D_1, D_2, D_3 to Form Training Data

		B_{total}	B_x	B_y	B_z	ϕ	θ
MAE	$D_1^{train} \rightarrow D_4^{test}$	193.680	146.010	124.783	136.892	5.497	9.009
	$D_2^{train} \rightarrow D_4^{test}$	246.086	160.538	131.986	186.657	6.296	9.501
	$D_3^{train} \rightarrow D_4^{test}$	231.481	153.664	129.813	173.582	5.823	7.473
	$D_{1,2}^{train} \rightarrow D_4^{test}$	198.832	143.087	123.287	146.410	5.363	8.729
	$D_{1,3}^{train} \rightarrow D_4^{test}$	204.086	143.244	123.685	148.227	5.284	7.925
	$D_{2,3}^{train} \rightarrow D_4^{test}$	201.117	137.369	119.157	162.063	5.713	7.577
	$D_{1,2,3}^{train} \rightarrow D_4^{test}$	207.075	148.718	127.467	146.775	5.674	8.679
PA	$D_1^{train} \rightarrow D_4^{test}$	75.0%	80.1%	86.2%	87.2%	91.3%	79.1%
	$D_2^{train} \rightarrow D_4^{test}$	54.9%	77.6%	83.7%	77.0%	87.7%	76.3%
	$D_3^{train} \rightarrow D_4^{test}$	71.0%	79.0%	83.9%	81.2%	89.5%	86.2%
	$D_{1,2}^{train} \rightarrow D_4^{test}$	72.9%	81.5%	86.2%	84.4%	91.0%	79.9%
	$D_{1,3}^{train} \rightarrow D_4^{test}$	67.8%	80.9%	85.6%	82.9%	91.3%	82.2%
	$D_{2,3}^{train} \rightarrow D_4^{test}$	72.6%	82.8%	87.2%	83.3%	88.7%	84.6%
	$D_{1,2,3}^{train} \rightarrow D_4^{test}$	70.9%	80.0%	84.8%	84.1%	90.7%	79.5%
R-squared	$D_1^{train} \rightarrow D_4^{test}$	0.841	0.884	0.777	0.736	0.776	0.807
	$D_2^{train} \rightarrow D_4^{test}$	0.805	0.876	0.808	0.710	0.770	0.794
	$D_3^{train} \rightarrow D_4^{test}$	0.769	0.867	0.763	0.687	0.785	0.824
	$D_{1,2}^{train} \rightarrow D_4^{test}$	0.843	0.882	0.797	0.731	0.776	0.819
	$D_{1,3}^{train} \rightarrow D_4^{test}$	0.832	0.881	0.781	0.733	0.782	0.834
	$D_{2,3}^{train} \rightarrow D_4^{test}$	0.835	0.894	0.788	0.714	0.780	0.821
	$D_{1,2,3}^{train} \rightarrow D_4^{test}$	0.830	0.875	0.796	0.738	0.782	0.822
PPMCC	$D_1^{train} \rightarrow D_4^{test}$	0.936	0.943	0.888	0.859	0.881	0.902
	$D_2^{train} \rightarrow D_4^{test}$	0.927	0.939	0.904	0.862	0.882	0.895
	$D_3^{train} \rightarrow D_4^{test}$	0.896	0.935	0.877	0.834	0.889	0.911
	$D_{1,2}^{train} \rightarrow D_4^{test}$	0.937	0.941	0.897	0.858	0.882	0.907
	$D_{1,3}^{train} \rightarrow D_4^{test}$	0.934	0.942	0.891	0.861	0.885	0.915
	$D_{2,3}^{train} \rightarrow D_4^{test}$	0.928	0.946	0.889	0.853	0.888	0.909
	$D_{1,2,3}^{train} \rightarrow D_4^{test}$	0.933	0.940	0.899	0.863	0.885	0.909
Outlier-difference	$D_1^{train} \rightarrow D_4^{test}$	19651	22317	16592	12950	21951	14265
	$D_2^{train} \rightarrow D_4^{test}$	19562	22361	16772	12988	21959	13705
	$D_3^{train} \rightarrow D_4^{test}$	19647	22125	16731	12956	21931	15124
	$D_{1,2}^{train} \rightarrow D_4^{test}$	19622	22333	16645	12922	21955	14305
	$D_{1,3}^{train} \rightarrow D_4^{test}$	19650	22277	16573	12967	21961	13425
	$D_{2,3}^{train} \rightarrow D_4^{test}$	19691	22072	16668	13004	21949	15841
	$D_{1,2,3}^{train} \rightarrow D_4^{test}$	19660	22313	16594	12970	21954	13645

REFERENCES

- Asensio Ramos, A., & de la Cruz Rodríguez, J. 2015, *A&A*, 577, A140, doi: [10.1051/0004-6361/201425508](https://doi.org/10.1051/0004-6361/201425508)
- Asensio Ramos, A., & Díaz Baso, C. J. 2019, *A&A*, 626, A102, doi: [10.1051/0004-6361/201935628](https://doi.org/10.1051/0004-6361/201935628)
- Auer, L. H., Heasley, J. N., & House, L. L. 1977, *SoPh*, 55, 47, doi: [10.1007/bf00150873](https://doi.org/10.1007/bf00150873)
- Borrero, J. M., Tomczyk, S., Kubo, M., et al. 2011, *SoPh*, 273, 267, doi: [10.1007/s11207-010-9515-6](https://doi.org/10.1007/s11207-010-9515-6)
- Cao, W., Goode, P. R., Ahn, K., et al. 2012, *Astronomical Society of the Pacific Conference Series*, Vol. 463, NIRIS: The Second Generation Near-Infrared Imaging Spectro-polarimeter for the 1.6 Meter New Solar Telescope, ed. T. R. Rimmele, A. Tritschler, F. Wöger, M. Collados Vera, H. Socas-Navarro, R. Schlichenmaier, M. Carlsson, T. Berger, A. Cadavid, P. R. Gilbert, P. R. Goode, & M. Knölker, 291
- Cao, W., Jing, J., Ma, J., et al. 2006, *PASP*, 118, 838, doi: [10.1086/505408](https://doi.org/10.1086/505408)
- Carroll, T. A., & Kopf, M. 2008, *A&A*, 481, L37, doi: [10.1051/0004-6361:20079197](https://doi.org/10.1051/0004-6361:20079197)
- Carroll, T. A., & Staude, J. 2001, *A&A*, 378, 316, doi: [10.1051/0004-6361:20011167](https://doi.org/10.1051/0004-6361:20011167)
- Collados, M. 2008, in *Ground-based and Airborne Telescopes II*, ed. L. M. Stepp & R. Gilmozzi (SPIE). <https://doi.org/10.1117%2F12.790105>
- del Toro Iniesta, J. C., & Ruiz Cobo, B. 1996, *SoPh*, 164, 169, doi: [10.1007/bf00146631](https://doi.org/10.1007/bf00146631)
- Frutiger, C., Solanki, S. K., Fligge, M., & Bruls, J. H. M. J. 2000, *A&A*, 358, 1109
- Galton, F. 1886, *The Journal of the Anthropological Institute of Great Britain and Ireland*, 15, 246, doi: [10.2307/2841583](https://doi.org/10.2307/2841583)
- Goode, P. R., & Cao, W. 2012, *Astronomical Society of the Pacific Conference Series*, Vol. 463, The 1.6 m Off-Axis New Solar Telescope (NST) in Big Bear, ed. T. R. Rimmele, A. Tritschler, F. Wöger, M. Collados Vera, H. Socas-Navarro, R. Schlichenmaier, M. Carlsson, T. Berger, A. Cadavid, P. R. Gilbert, P. R. Goode, & M. Knölker, 357
- Goodfellow, I. J., Bengio, Y., & Courville, A. C. 2016, *Deep Learning, Adaptive computation and machine learning* (MIT Press). <http://www.deeplearningbook.org/>
- Lagg, A., Woch, J., Krupp, N., & Solanki, S. K. 2004, *A&A*, 414, 1109, doi: [10.1051/0004-6361:20031643](https://doi.org/10.1051/0004-6361:20031643)
- Landi Degl'Innocenti, E. 1984, *SoPh*, 91, 1, doi: [10.1007/bf00213606](https://doi.org/10.1007/bf00213606)
- Landolfi, M., Landi Degl'innocenti, E., & Arena, P. 1984, *SoPh*, 93, 269, doi: [10.1007/bf02270839](https://doi.org/10.1007/bf02270839)
- LeCun, Y., Bengio, Y., & Hinton, G. 2015, *Nature*, 521, 436, doi: [10.1038/nature14539](https://doi.org/10.1038/nature14539)
- Liu, C., Cao, W., Chae, J., et al. 2018, *ApJ*, 869, 21, doi: [10.3847/1538-4357/aaecd0](https://doi.org/10.3847/1538-4357/aaecd0)
- McHugh, M. L. 2012, *Biochemia Medica*, 22, 276, doi: [10.11613/bm.2012.031](https://doi.org/10.11613/bm.2012.031)
- McMullin, J. P., Rimmele, T. R., Keil, S. L., et al. 2012, in *Ground-based and Airborne Telescopes IV*, ed. L. M. Stepp, R. Gilmozzi, & H. J. Hall (SPIE). <https://doi.org/10.1117%2F12.926949>
- Pearson, K. 1895, *Proceedings of the Royal Society of London*, 58, 240, doi: [10.1098/rspl.1895.0041](https://doi.org/10.1098/rspl.1895.0041)
- Press, W. H., Flannery, B. P., Teukolsky, S. A., & Vetterling, W. T. 1991, *Mathematics of Computation*, 56, 396, doi: [10.2307/2008560](https://doi.org/10.2307/2008560)
- Quintero Noda, C., Asensio Ramos, A., Orozco Suárez, D., & Ruiz Cobo, B. 2015, *A&A*, 579, A3, doi: [10.1051/0004-6361/201425414](https://doi.org/10.1051/0004-6361/201425414)
- Rees, D., Guo, Y., López Ariste, A., & Graham, J. 2004, in *Lecture Notes in Computer Science* (Springer Berlin Heidelberg), 388–394. https://doi.org/10.1007%2F978-3-540-30134-9_52
- Ruiz Cobo, B., & Asensio Ramos, A. 2012, *A&A*, 549, L4, doi: [10.1051/0004-6361/201220373](https://doi.org/10.1051/0004-6361/201220373)
- Ruiz Cobo, B., & del Toro Iniesta, J. C. 1992, *ApJ*, 398, 375, doi: [10.1086/171862](https://doi.org/10.1086/171862)
- Sen, A., & Srivastava, M. 1990, *Regression Analysis* (Springer-Verlag New York), doi: [10.1007/978-1-4612-4470-7](https://doi.org/10.1007/978-1-4612-4470-7)
- Skumanich, A., & Lites, B. W. 1987, *ApJ*, 322, 473, doi: [10.1086/165743](https://doi.org/10.1086/165743)
- Socas-Navarro, H. 2003, *Neural Networks*, 16, 355, doi: [10.1016/s0893-6080\(03\)00024-8](https://doi.org/10.1016/s0893-6080(03)00024-8)
- . 2005, *ApJ*, 621, 545, doi: [10.1086/427431](https://doi.org/10.1086/427431)
- Socas-Navarro, H., López Ariste, A., & Lites, B. W. 2001, *ApJ*, 553, 949, doi: [10.1086/320984](https://doi.org/10.1086/320984)
- Teng, F. 2015, *SoPh*, 290, 2693, doi: [10.1007/s11207-015-0781-1](https://doi.org/10.1007/s11207-015-0781-1)
- Unno, W. 1956, *Astronomical Society of Japan*, 8, 108
- Wang, H., Cao, W., Liu, C., et al. 2015, *Nature Communications*, 6, doi: [10.1038/ncomms8008](https://doi.org/10.1038/ncomms8008)
- Wang, H., Liu, C., Ahn, K., et al. 2017, *Nature Astronomy*, 1, doi: [10.1038/s41550-017-0085](https://doi.org/10.1038/s41550-017-0085)
- Xu, Y., Cao, W., Ding, M., et al. 2016, *ApJ*, 819, 89, doi: [10.3847/0004-637x/819/2/89](https://doi.org/10.3847/0004-637x/819/2/89)
- Xu, Y., Cao, W., Ahn, K., et al. 2018, *Nature Communications*, 9, doi: [10.1038/s41467-017-02509-w](https://doi.org/10.1038/s41467-017-02509-w)